**ORIGINAL PAPER**

# SQUIDs for magnetic and electromagnetic methods in mineral exploration

Ronny Stolz[1] · Markus Schiffler[1] · Michael Becken[2] · Anneke Thiede[2] · Michael Schneider[3] ·
Glenn Chubak[4] · Paul Marsden[5] · Ana Braña Bergshjorth[6] · Markus Schaefer[7] · Ockert Terblanche[8]

**Abstract**

Research on quantum sensors for the detection of magnetic fields (quantum magnetometers) is one of the fast-moving areas of Quantum Technologies. Since there exist expectations about their use in geophysics, this work will provide a brief overview on the various developing quantum technologies and their individual state of the art for implementing quantum magnetometers. As one example, the developments on superconducting quantum interference devices, so-called SQUIDs as a specific implementation of a quantum magnetometer, are presented. In the course of this, SQUID instrument implementations and associated demonstrations and case studies will be presented. An airborne vector magnetometer with ultra-low noise ($< 10 \mathrm{fT}/\sqrt{\mathrm{Hz}}$) and high dynamic range of $> 32$bit will be introduced which has the prospect to be applied for the magnetic method in parallel with electromagnetic methods such as passive audio-frequency magnetics or semi-airborne methods using active transmitters such as elongated grounded dipole sources. The according signals are separated in the frequency domain. A second implementation is an airborne full tensor gradiometer instrument will be discussed which has shown already a number of successful case studies and which turned into commercial operation in the past years. Besides the airborne instrument, a very successful implementation of quantum magnetometers is the SQUID-based receiver for the ground-based transient electromagnetic method. Today it is a mature technology which has been in commercial use for more than a decade and has led to a number of discoveries of conductive ore bodies. One case study will be presented which demonstrates the performance of this instrument. Finally, future prospects of using quantum magnetometers, including SQUIDs and new optically pumped magnetometers, in geophysical exploration will be discussed. Particular applications for both sensor types will be introduced.

**Keywords** Mineral exploration · Magnetics · Electromagnetic methods · Quantum sensors · SQUID

✉ Ronny Stolz
   ronny.stolz@leibniz-ipht.de

1  Department Quantum Systems, Leibniz Institute of Photonic Technology, Albert-Einstein-Str. 9, 07745 Jena, Germany

2  Institute of Geophysics, University of Münster, Corrensstr. 24, 48149 Münster, Germany

3  Supracon AG, An der Lehmgrube 11, 07751 Jena, Germany

4  DIAS Geophysical Ltd, 2131 Airport Drive, Saskatoon, SK S7L 7E1, Canada

5  Nordic Iron Ore AB, Vendevägen 85A, 182 91 Danderyd, Stockholm, Sweden

6  Nordika Geophysics, Björnebergsvägen 58, 55448 Jönköping, Sweden
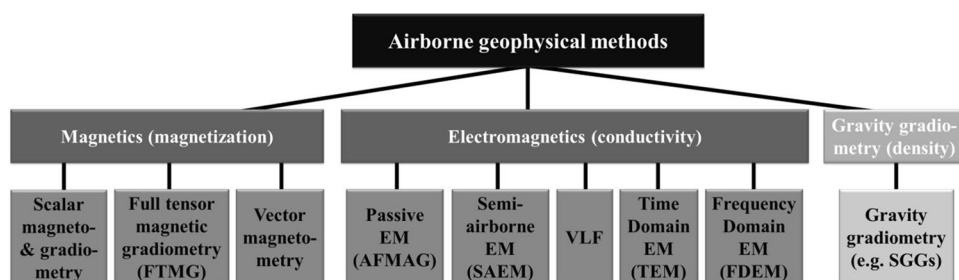
7  Johannesburg, South Africa

8  AngloGold Ashanti, 140 St Georges Terrace, Perth, WA 6010, Australia

## Background

Until the 2000s, most of the discoveries of mineral resources are underneath a cover of 100–200 m, but in the past few years a significant demand for increasing investigation depth (Schodde 2017) is observable in parallel with performing quick, cost- and time-efficient as well as environment friendly programs for raw mineral exploration. In some cases, the hunt for mineral resources must be performed in terrains with rough climate conditions or with demanding topography or limited access (swamps).

About 1070 discoveries have been made worldwide within the last decade. However, only 19 of them were

**Fig. 1** Airborne exploration methods which may benefit from the application of quantum sensors. The abbreviation AFMAG corresponds to the audio-frequency magnetic method. In this article, the gravimetric method will not be covered

**Airborne geophysical methods**

**Magnetics (magnetization)**
- Scalar magneto- & gradiometry
- Full tensor magnetic gradiometry (FTMG)
- Vector magnetometry

**Electromagnetics (conductivity)**
- Passive EM (AFMAG)
- Semi-airborne EM (SAEM)
- VLF
- Time Domain EM (TEM)
- Frequency Domain EM (FDEM)

**Gravity gradiometry (density)**
- Gravity gradiometry (e.g. SGGs)

classified as world class or "Tier 1" deposits[1]; four of them were discovered each in China and Australia, three in each of Africa and Canada, two of them each in the USA and Pacific/Southeast Asia as well as one in Latin America (Schodde 2019). In order to meet all the earlier listed demands at the same time, magnetic and electromagnetic (EM) methods making use of quantum sensors with exceptional sensitivity and resolution are very promising for future exploration scenarios. In the long term, gravimetry using quantum sensors will also play a role in exploration.

Over the years, various reviews were undertaken to report on state of the art and new developments in most important methods for metalliferous mining geophysics such as Fullagar and Fallon (1997), Nabighian and Asten (2002), or Vallée et al. (2011). They also provide some discussion of new sensor developments.

The *magnetic method* is still one of the most popular and intensively used methods in mineral exploration. The reviews by Nabighian et al. (2005), Vallée et al. (2011), and lately Hinze et al. (2013) with included references provide a substantial overview on this method, the sensors used, the instrumentation, and data acquisition as well as according processing and interpretation techniques. State of the art sensors (Grosz et al. 2017) for the airborne magnetic method are scalar-type magnetic field sensors, called magnetometers, such as optically pumped magnetometers (OPMs) or vector-type magnetometers such as fluxgates. Scalar-type magnetometers measure the amplitude of the Earth's magnetic field, also called total magnetic field intensity (TMI), by making use of the Zeeman effect in alkali atom vapor (most often cesium) enclosed in glass cells. The best commercially available OPMs (Commercial OPM providers 2020) achieve a white noise floor of about $0.3 \mathrm{pT}/\sqrt{\mathrm{Hz}}$ in a bandwidth of < 10Hz. OPMs in scalar magnetometry, left lower box in Fig. 1, suffer so-called dead zones and heading errors (GEM

Systems Inc., 2020) which makes their response sensitive to their orientation (internally it relates to the direction of the light path through the glass cell and orthogonal to it) in the external magnetic field. Multiple sensors may be arranged to enable scalar gradiometry (Hogg 2004).

Fluxgate magnetometers (FGMs) have a main sensitive axis along the internal core of highly permeable material and measure the corresponding magnetic field component. The best commercial fluxgates provide a white noise floor of $\approx 1 \mathrm{pT}/\sqrt{\mathrm{Hz}}$ with bandwidths of about 1–25 kHz, e.g., Bartington instruments Ltd. (2020). However, they exhibit a significant increase of the noise spectra for low frequencies of < 10Hz. There is also progress in research towards FGMs with higher resolution. This is reviewed in Grosz et al. (2017) and the included references. Three orthogonal FGMs would thus enable vector magnetometry (Christensen and Dransfield 2002), see Fig. 1.

The state of the art of the quantum sensors will be reviewed in the "Short review on quantum sensing" section. Special focus is laid on superconducting quantum interference devices, so-called SQUIDs in the "Superconducting quantum magnetometers" section.

*Electromagnetic methods* have been successfully used since the 1920s as a toolset for sensing conductive bodies or conductance contrasts in rock materials and can thus be used to explore the sub-surface for certain mineral deposits (Grant and West 1965; Nabighian 1991; Zhdanov 2010; Smith 2014). These methods acquire an electromagnetic response excited by natural or artificial sources either in the frequency (FD) or time domain (TD). These electromagnetic (EM) source fields interact with conductive structures and lead to secondary responses which are often of very weak amplitude and demand magnetic field sensors, so-called magnetometers, of utmost sensitivity and low noise. This leads to a large ratio between the amplitude of the excitation signal and the noise which is a measure of the signal to noise ratio *SNR*, which should be covered by the sensing instrument and the associated data acquisition system. Thus, 24-bit digitizers are today state of the art. The demand of the high *SNR* was significantly increased by the tremendous improvements in the EM methods achieved by both the

---

[1] According to Schodde (2017), "Tier 1" deposits are large volume, long life, and low cost with NPV of > 1 billion US$; "Tier 2" deposits are "significant" but have an NPV of 0.2 to 1 billion US$; "Tier 3" deposits are modest or marginal deposits, with an NPV of up to 0.2 billion US$.

industry and the academia, in the past decade, namely by increasing the transmitting power (for the active EM methods) and the resolution of the sensing instruments, developing new operating platforms and according peripheral instrumentation. Quantum sensors may in this context play an important role to gain an improved *SNR* which e.g. facilitates more robust observations at late acquisition times, very low frequencies, or at large transmitter–receiver separations and is thus the pathway to increase exploration depths. The higher resolution of sensing instruments is also beneficial for natural source EM measurements, where the signal amplitude is even weaker compared to active source methods.

All the listed advances and new software toolchains for the forward modeling and inversion of EM data using state of the art computing facilities lead to improved Earth models describing the 3D distribution of conductivities of rocks which may vary over several orders of magnitude. For example, graphite or sulfide bearing structures can give rise to significant conductivity anomalies, hydrothermal alteration zones can exhibit elevated conductivity, and conductive clay caps are indicative of geothermal reservoirs. Furthermore, geotechnical applications such as the detection of pipes, foundations, or unexploded ordnances are possible targets for electromagnetic methods. By increasing the *SNR*, even more subtle EM features can be detected which will help to decipher other physical or chemical phenomena in sub-surface geological structures alike superparamagnetism (Macnae 2016b, 2017) and induced polarization (IP; Kaminski and Viezzoli 2017; Macnae 2016a).

To date, the plurality of those EM instruments uses induction coils (abbreviated as "coils" herein) of various sizes ranging from centimeters to hundreds of meters. FGMs or OPMs are also used for some instruments or complement coil instruments for EM field measurement at very low frequencies.

### Airborne electromagnetic methods

The introduced EM methods are widely used in mineral exploration during airborne, submarine and marine, onshore and borehole surveys, respectively. Airborne electromagnetic methods (AEM) as one topic of this article provide a cost- and time-effective operation also in areas with critical environmental conditions, e.g., swamp, or the lack of access permission. Legault (2015) provides a recent overview on state of the art and future directions of AEM methods. In order to increase the investigation depth further, also semiairborne EM methods (SAEM) using airborne receivers and ground-based transmitters or vice versa are currently under development. Examples for implementing the SAEM method are discussed in detail e.g. by Wu et al. (2019) or Steuer et al. (2020).

This work will provide a short insight how AEM methods may benefit from the application of quantum sensors (QS) namely SQUIDs from today's perspective. A detailed review on the use of SQUIDs in geophysics is given by Stolz et al. (2021b). Figure 1 lists all airborne magnetic, gravimetric, and AEM methods which may use quantum sensor instrumentation in future.

### Structure of the paper

The first section provides the background information for this article. The "Short review on quantum sensing" section introduces the quantum sensors, and the "Airborne superconducting QS instruments" section focusses on first realizations of airborne QS instrumentation. Therein, the according systems are introduced. They are either close to the threshold of being in operation or already in commercial use. One key concept is to reduce the motion noise of the airborne platform for the successful operation of the QSs. This topic will also be introduced and discussed towards the end of this section. Therein, validation studies performed with two QS instruments on helicopter-based platforms will be drawn. The "Performance evaluation and demonstrations of the airborne SQUID instruments" section demonstrates a ground-based application of SQUID instruments in mineral exploration based on the time domain EM method. It is now a standard method in industry and a number of instruments are in operation. One case study proves the performance and advantages of these QS instruments in mineral exploration. Finally, the work is concluded and a short outlook provides insights of the next steps of the recent QS instrument development.

## Short review on quantum sensing

### Generals

The quantum technologies (QTs) were initiated by Max Planck and Albert Einstein almost 120 years ago. Today, the megatrend in R&D worldwide is to develop the QTs to solve a number of challenges of our society. Hereafter, a distinction between the first and second generation of QTs respectively QT 1.0 and 2.0 is made, refer to Appendix 1.

In this section especially, the quantum sensing of the magnetic field at highest resolution by quantum magnetometers (QMs) will be reviewed and future trends introduced. Most of them still represent only the QT1.0 such as SQUIDs or the new developments in optically pumped magnetometers (OPMs) or sensors based on nitrogen vacancies in diamond (NVCD). First developments in QT2.0 are ongoing and will be presented hereafter.

Prior to the presentation of quantum magnetometer technologies, the framework of the evaluation of the various sensors has to be set. The successful industrial use mostly requires low costs of acquisition and operation of the

**Fig. 2** LTS SQUID–based gradiometers and magnetometers on the left- and right-hand panel, respectively
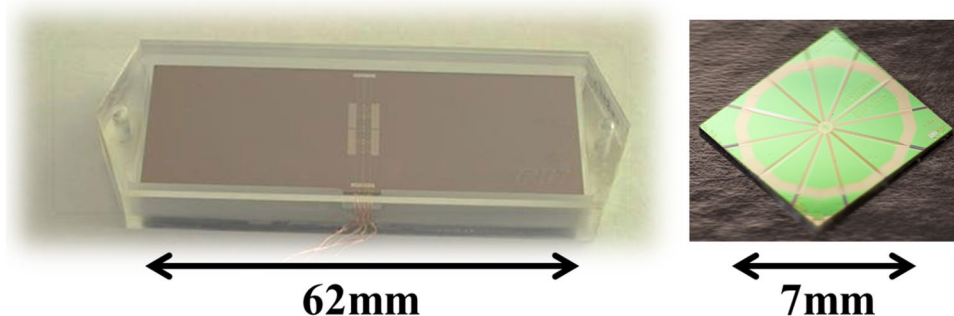


instruments. Besides this, the suitability for the particular measurement task has to be considered such as limitations set by space, weight, and power supply, scanning speed, ambient noise conditions (e.g., of autonomous vehicles), and availability of liquid coolants (for superconducting sensors) which are often convolved with the platform to be used (e.g., Liu et al. 2022). The success of an operation is highly dependent on the performance-specific parameters of the magnetometers, such as intrinsic sensor noise, cross-talk, linearity, slew rate, dynamic range, and bandwidth. These parameters and conventional magnetic field sensors are briefly introduced in Appendix 2.

## Superconducting quantum magnetometers

The SQUID as QS evolved within the past five decades after their invention by Jaklevic et al. (1964). It exploits various physical phenomena effects such as superconductivity, the Meissner-Ochsenfeld effects, the Josephson effects, and use quantum effects on the macroscopic scale, such as macroscopic wave functions, quantum interference, and quantum mechanical tunneling (Clarke and Braginski 2004). The generic design of a SQUID is a ring of superconducting material which is interrupted either by one or by two Josephson junctions for RF or DC SQUIDs respectively. The DC SQUIDs are today the favorite implementation due to its simple readout and control.

SQUIDs have become a mature technology to be used in geoscientific applications (Stolz et al. 2021b). In the context of this work, SQUIDs are divided into two classes: low-temperature (LTS) and high-temperature (HTS) SQUIDs being immersed in liquid helium (lHe, 4.2K) or liquid nitrogen (lN$_2$, 77K), respectively. There were great achievements in electrically powered refrigeration, aka cryo-coolers, which are still not used for magnetically unshielded measurement due to power restrictions and noise created by the devices.

SQUID magnetometers provide extremely low white noise floor of well below $1fT/\sqrt{Hz}$, a high slew rate of up to $\sim 250mT/s$ (Stolz et al. 2021b), a relative magnetic field measurement due to the use of a feedback electronics (Drung and Mück 2004), a wide-band frequency-independent transfer function (DC to $> 10GHz$), and a single sensitive axis. These exceptional values often relate to the SQUIDs itself. When implemented in instruments, these parameters are often not achieved since noise, linearity, and slew rate are mainly limited by the room-temperature feedback electronics for readout and thus depend on the various providers.

This QS technology has a specific feature: the flux quantization causes a periodic voltage to magnetic field characteristics of the SQUID which allows for readout schemes with extreme linearity and *SNR*. Stolz et al. (2021b) introduce and discuss these various readout schemes such as flux-counting, fast resetting, flux ramp modulation, hybrid or cascade SQUIDs, or even purely digital SQUIDs.

The QS instrumentation which will be introduced in the subsequent sections of this article makes use of the SQUIDs fabricated in the author's organization. Figure 2 depicts the two SQUID types used inside of the described instruments.

Superconducting circuits also allow for the realization of two-state systems (also called two-level systems as the simplest quantum system which can exist only in one of the two states or a superposition of them). They are used for the realization of quantum bits, so-called qubits, for next-generation quantum computers. These structures can also be tuned for quantum magnetic field sensing using metrological readout schemes. Early implementations of this design provide sensitivities of $\sim 20pT/\sqrt{Hz}$ (Danilin et al. 2018) and $\sim 3.3pT/\sqrt{Hz}$ at 10MHz (Bal et al. 2012). However, these new magnetometers of the QT2.0 require ultra-low temperatures of tens of milli-Kelvins.

## Optically pumped magnetometers

OPMs, also belonging to the QT1.0, make use of optical spectroscopy on an alkali vapor enclosed in transparent cells, cf. Figure 3. The state of the art and future developments are reviewed and discussed in detail by Budker and Jackson Kimball (2013). With the advent of the funding towards the QTs, significant progress in the OPMs has been achieved. New readout schemes, new implementations of vapor cells such as microelectromechanical-(MEMS-)like

**Fig. 3** Generic setup of an Mx-type OPM (Budker and Jackson Kimball 2013). The RF magnetic field is used to tune the response of the OPM to the optical resonance. According to the Zeeman effect, it corresponds to the Larmor frequency which is proportional to the amplitude of the magnetic field vector
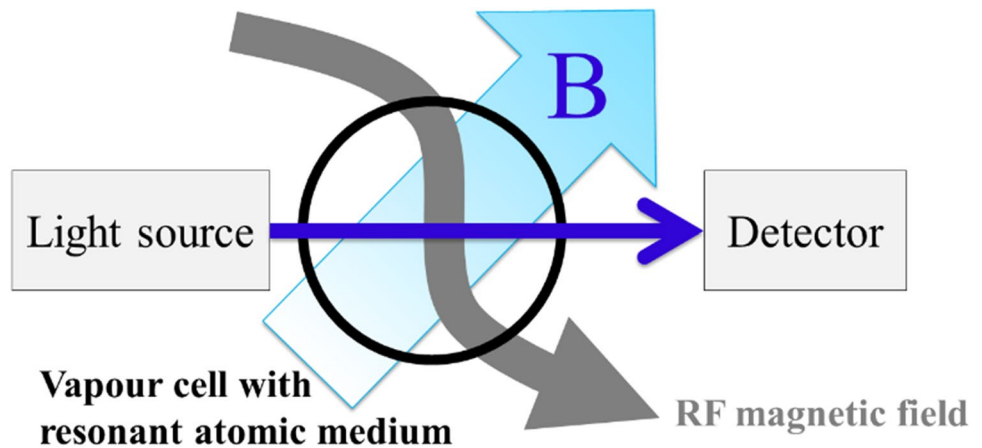
integration technologies, and new low-noise laser sources have all contributed to very low-noise quantum magnetometers going beyond the known state of OPMs (Commercial OPM providers 2020). OPMs are still scalar-type sensors with dead zones and heading errors leading to issues during magnetically unshielded operation (Oelsner et al. 2019b; Limes et al. 2020). New concepts for reducing these effects are currently under investigation. In the latest publications, the performance of OPMs successively improves for miniaturized cells, e.g., R. Zhang et al. (2021a, b), Gerginov et al. (2020), Oelsner et al. (2019a, b) and for larger cell volumes, e.g., Zhang et al. (2020a), Limes et al. (Gerginov et al.; 2020), Zhang et al. (2020b), and references therein. A first demonstration of OPMs operating in the Earth magnetic field and recording signals from a distant transmitter with a system noise floor of $\sim 80\,\mathrm{fT}/\sqrt{\mathrm{Hz}}$ in a bandwidth of $\sim 800\,\mathrm{Hz}$ was reported by Schultze et al. (2017).

In order to broaden the potential use cases of OPMs, the question is whether OPM can also be designed as vector-type sensors. Various concepts, for examples refer to references 17–25 in R. Zhang et al. (2021a, b), have been investigated. This would enable software gradiometers (differencing of individual sensor signals) but also leads to an extremely high *DR* since the individual sensors with low noise are moved through the Earth's magnetic field. As a consequence, a number of groups are working on hardware gradiometers such as Lucivero et al. (2021), Perry et al. (2020), and Schwindt (2019). The best reported (Lucivero et al. 2021) gradient noise is $\sim 1\,\mathrm{pT}/\left(\mathrm{m} \cdot \sqrt{\mathrm{Hz}}\right)$. For a comparison of this noise floor to other gradient sensors, refer to (Stolz et al. 2021a). Another operational limitation of OPMs is also the limited bandwidth compared to SQUIDs.

In the end, OPMs are on the cusp of moving quantum magnetometers into real-world applications of geophysics without the hurdle of cryogenic operation and reduced low frequency noise. They would outperform conventional OPMs and support new exploration methods with autonomous platforms.

## Color center sensors

This type of quantum magnetometers uses defects in the lattice of solids. The most investigated types of defects are those in diamond called nitrogen-vacancy centers (NVCD). It comprises two adjacent places in the lattice of the diamond where carbon atoms are missing; one is replaced by a nitrogen atom, and the other is left empty, c.f. Figure 4. The missing bonds in the structure cause the according electrons to be extremely sensitive to environmental variations. The NVCD magnetometers do need no cryogenics and are easy
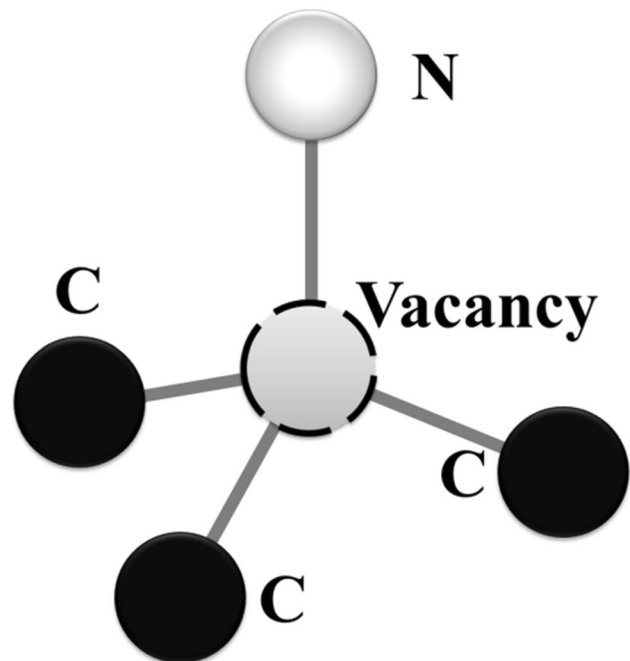
**Fig. 4** Nitrogen vacancy in the diamond lattice

**Table 1** Comparison matrix of available SQUID-based TEM receiver instruments

| | Quantum magnetometer | | | | | Conventional | |
|---|---|---|---|---|---|---|---|
| | SQUID ML7[(1)] | SQUID[(2)] (airborne) | OPM | NVCD | Cold atom | Fluxgate | OPM[(3)] |
| White noise floor $B_{\text{noise,rms}}$ (fT/$\sqrt{\text{Hz}}$) Lab/field testing | 0.7/1.3 | 4.5/>10 | 80 | $2.6\times10^3$ | $8.3\times10^3/330\times10^3$ | $1\times10^3$ | 350 |
| Bandwidth $f_{\text{3dB}}$ (MHz) | 8.0/0.1[(4)] | 1.5/0.1[(4)] | $0.8\times10^{-3}$ | 200 | 0.1 | $3\times10^{-3}$ | $\approx50\times10^{-6}$ |
| Dynamic range (dB/bit) | 165/27.1 | >194/>32 | 137.3/22.5 | n.a | | 115.7/19.0 | 136.6/22.4 |
| Details, references | [1] | [2] | [3] | [4] | [5] | [6] | [7] |

*[(1)]Ground-based TEM instrument, refer to the "Ground-based TEM with SQUIDs" section

*[(2)]Flux counting electronics used for SQUID readout, refer to Stolz et al. (2021b)

*[(3)]Parameters based on G-824A of Geometrix

*[(4)]Bandwidth: sensor with electronics/complete receiver unit

[1], slew rate 5–10mT/s, Schmelz et al. (2012), Chwala et al. (2013)

[2], slew rate 0.7mT/s, Larnier et al. (2021)

[3], max. range ±100µT, Schultze et al. (2017)

[4], C. Zhang et al. (2021a, b)

[5], max. range ±14.2µT, Vengalattore et al. (2007), Cohen et al. (2019)

[6], max. range ±100µT, Bartington instruments Ltd. (2020), Janosek et al. (2020)

[7], Commercial OPM providers (2020)

to be read out with laser light. The best reported intrinsic magnetic field noise is $\sim 2.6$pT/$\sqrt{\text{Hz}}$ (C. Zhang et al. 2021a, b) and 0.9pT/$\sqrt{\text{Hz}}$ for a 20kHz AC field (Wolf et al. 2015). While this magnetometer type is capable for microscopic magnetic imaging, significant progress is required to realize sensitive enough magnetometers ($< 100$fT/$\sqrt{\text{Hz}}$) for geophysical applications.

## Cold-atom-type sensors

The advantages in the past decades on producing, trapping, and manipulating cold atoms (alkali species) enable highly sensitive, spatially resolved magnetic field measurements. Three variants based on density modulations, spinor condensates, or optical lattices are under investigation (Budker and Jackson Kimball 2013). Up to now, magnetic field noise levels of $\sim 10$pT/$\sqrt{\text{Hz}}$ have been demonstrated (Koschorreck et al. 2011; Venturelli 2018) and $\sim 8.3$pT/$\sqrt{\text{Hz}}$ (Vengalattore et al. 2007) for bulky laboratory setups. Koschorreck et al. (2011) postulate a sub-pT ($\sim 300$fT/$\sqrt{\text{Hz}}$) noise figure and recently Chai et al. (2022) claim a 10-fT resolution using superconducting flux concentrators in the future. However, significant effort is still required to build robust enough and small-sized instruments with this technology.

## Magnetometer comparison

The following table summarizes the recently published parameters of quantum magnetometers and conventional magnetic field sensing technologies.

The slew rate is specified for only the SQUID instruments. With exception of the measured values for the SQUID instruments, the dynamic range is calculated based on the white noise figure during the field testing using $DR = 20\log_{10}\left[B_{\text{max}}/\left(B_{\text{noise,rms}} \bullet k\right)\right]$. The factor $k$ is the product of a Crest factor of 6 (Motchenbacher and Fitchen 1973) and the square root of the signal bandwidth given in Table 1.

## Airborne superconducting QS instruments

In this section, the various SQUID-based instruments for airborne methods in exploration developed and implemented by the authors will be introduced and field data are used to validate their maturity for geophysical airborne applications. For comparison, the status of independent SQUID instrument developments worldwide is discussed by Stolz et al. (2021b).

## Airborne full tensor magnetic gradiometry

The history and future perspectives of full tensor magnetic gradiometry (FTMG) are discussed lately by Stolz et al. (2021a). Herein, we will only briefly introduce the QMAG$^T$ instrument which was formerly called JESSY STAR. It is designed to measure the complete gradient of the Earth's magnetic field $\widehat{B}$ which forms a second-rank tensor with nine components $B_{ik} = \partial B_i / \partial x_k$ ($i, k \in x, y, z$):

$$\widehat{B} = \begin{pmatrix} B_{xx} & B_{xy} & B_{xz} \\ B_{yx} & B_{yy} & B_{yz} \\ B_{zx} & B_{zy} & B_{zz} \end{pmatrix} = \begin{pmatrix} B_{xx} & B_{xy} & B_{xz} \\ B_{xy} & B_{yy} & B_{yz} \\ B_{xz} & B_{yz} & -B_{xx}-B_{yy} \end{pmatrix}. \quad (1)$$

In assumption of quasi-stationary conditions and the current flow in the sub-surface to give negligible responses, only a set of five independent components (e.g., dependent components highlighted in gray on the right-hand side of Eq. 1) exists. Six of the introduced planar-type first-order gradiometer SQUIDs are arranged on a stump of a 6-sided pyramid, similar to the arrangement in Ludwig et al. (1990), in order to measure the gradient tensor. Any selection of five gradiometer signals is sufficient to derive all required five tensor components honoring the Laplace condition $\sum_{i=1}^{3} B_{ii} = 0$. If all six sensors provide good data quality, the additional signal can be used for denoising. The methods for an appropriate consideration of the properties of the magnetic gradient tensor (i.e., the cross-coupling between different gradient tensor components, tensorially consistent microlevelling and interpolation, and use of the rotational invariants of the tensor) are presented in FitzGerald and Holstein (2006) and later implemented by Schiffler (2017). As reference for the homogeneous magnetic field, a 3D vector magnetometer (3D-VM) is implemented by three small-sized magnetometer SQUIDs (outer diameter $\sim 140\mu m$). Their signals are used to improve the quality of the FTMG data further (refer to Stolz et al. 2006). According to the discussion on intrinsic vs. system noise, the semiconductor-based readout electronics still limits the overall system's noise to $\sim 100 - 200\text{fT}/\left(\text{m} \bullet \sqrt{\text{Hz}}\right)$ and also the *SNR* (Stolz et al. 2020). In future, the readout principle introduced for the vector magnetometer instrument which uses the periodic characteristics of the SQUID will overcome these limitations for system noise and SNR.

The whole sensor head is immersed in liquid helium inside a plastic cryostat (cooling unit) with diameter of 15.8cm and height of 60cm. The cryostat has to be refilled every third day with $\sim 8l$ of liquid helium. A new cryostat generation is in development for much longer refill intervals. The instrument weighs about $\sim 30kg$ and is thus not simply deployable on a drone. The recent operations are performed in a towed bird, introduced later herein, or stinger from a helicopter or fixed-wing installation on an aircraft.

The QMAG$^T$ instrument is further complemented with a small-size data acquisition instrument including the batteries for power supply, state of the art 24-bit ADCs (also for other peripheral sensors), a differential GPS (dGPS) receiver, a high-performance inertial measurement unit (IMU implementing three optical gyroscopes and three MEMS accelerometers; refer to technology review by El-Sheimy and Youssef 2020), a radar and/or laser altimeter, and according tools for real-time system control and data acquisition. A software toolset based on Matlab™ scripts allows for post-processing,[2] quality control, inversion, and interpretation of data (Schiffler et al. 2014, 2017; Schiffler 2017).

## Airborne vector magnetometry

The application of a 3D-VM is a much greater challenge than traditional TMI measurements in magnetics. Although tri-axial vector magnetometers are deployed on most airborne TMI survey systems, they are in most cases only used for denoising of the TMI channels (Christensen and Dransfield 2002). Using the ability of the SQUID instruments to track the individual components of the Erath magnetic field vector, a second airborne SQUID-based instrument is under development enabling to extract the magnetic field vector and transfer functions for passive EM methods based on frequency content (magnetic and EM signatures for frequencies below and above 5Hz, respectively). It is called QAMT (quantum sensor–based system for audio-frequency-MT) and has a similar data acquisition system, the same peripheral components, and is housed in a cryostat with the same dimensions but longer operation time of up to 7 days without refill. Three of the already introduced ML7-type SQUID magnetometers are used in conjunction with a fast-resetting readout electronics which also limits the system's noise floor to $\sim 5\text{fT}/\sqrt{\text{Hz}}$ (which is more than five times higher than the intrinsic noise). They are arranged orthogonal to each other to implement a 3D-VM. The electronics uses up to a 1-MHz clock frequency and enables a *DR* of 32bit with a slew rate of $\sim 0.7\text{mT/s}$ (refer to Table 1).

The passive 3D-VM instrument has been used extensively in semi-airborne EM (SAEM) applications, where the primary and secondary magnetic fields due to the injection of a high-power alternating current into the ground are recorded

---

[2] The post-processing includes synchronization of the various data streams using PPS signal of the GPS receiver, the compensation of the influence of the homogeneous Earth magnetic field called balancing, the un-mixing of the tensor components, the IMU data processing and rotation of the tensor into an Earth-fixed Earth-centered coordinate system, subsequent compensation, tensor-consistent micro-leveling, and interpolation. Those steps are introduced by Schiffler (2017). Additionally, the TMI is calculated (Schiffler et al. 2014) and if required tensor components are transformed (Schiffler 2017). The application of the inversion is described by Queitsch et al. (2019).

during overflights of one or multiple transmitter footprints. From the data, frequency-domain transfer functions $\mathbf{T}_I$ that relate the individual components to the source current as

$$
\begin{pmatrix} B_x \\ B_y \\ B_z \end{pmatrix}(\omega, \boldsymbol{r}) = \mathbf{T}_I(\omega, \boldsymbol{r})\boldsymbol{I}(\omega). \tag{2}
$$

are estimated, where $\mathbf{T}_I$ is of dimension $3 \times 1$, refer to Becken et al. (2020) for details:

In AFMAG field operations, another SQUID-based 3D-VM instrument (Chwala et al. 2013), optionally complemented with electric field measurements, is synchronously operated on the ground in parallel to the airborne instrument. together with an electrode array for recording of the horizontal electric field components as a ground base station. This facilitates the estimation of the spatial distribution of the $1 \times 2$ vertical magnetic transfer functions $\mathbf{T}_z$ from the frequency-domain relation

$$
B_z(\omega, \boldsymbol{r}) = \mathbf{T}_z(\omega, \boldsymbol{r})\begin{pmatrix} B_x \\ B_y \end{pmatrix}(\omega, \boldsymbol{r}). \tag{3}
$$

just from the airborne instrument at position $\boldsymbol{r}$, or the estimation of inter-station vertical and horizontal magnetic transfer functions (i.e., the horizontal magnetic tensor $\mathbf{T}_h$) relating the three magnetic components recorded airborne to the horizontal magnetic field components recorded at the ground station at position $\boldsymbol{r}_0$

$$
B_z(\omega, \boldsymbol{r}) = \mathbf{T}_z(\omega, \boldsymbol{r}|\boldsymbol{r}_0)\begin{pmatrix} B_x \\ B_y \end{pmatrix}(\omega, \boldsymbol{r}_0), \tag{4}
$$

$$
\begin{pmatrix} B_x \\ B_y \end{pmatrix}(\omega, \boldsymbol{r}) = \mathbf{T}_h(\omega, \boldsymbol{r}|\boldsymbol{r}_0)\begin{pmatrix} B_x \\ B_y \end{pmatrix}(\omega, \boldsymbol{r}_0). \tag{5}
$$

Both SAEM and AFMAG are frequency-domain methods that operate in similar audio-frequency ranges.

The first successful demonstration of this instrument was undertaken at the Vredefort impact crater in the Republic of South Africa in 2020 (Larnier et al. 2021).

# Performance evaluation and demonstrations of the airborne SQUID instruments

In this section, we report on the latest investigations and demonstrations performed with the various SQUID-based instruments for airborne methods in exploration.

## Demonstrations at Bad Grund, Germany

In this more R&D-related study, the airborne SQUID-based QAMT instrument underwent demonstrations for two

geophysical methods — the SAEM method and AFMAG. Since this instrument implements a vector magnetometer, motion noise of the platform is the main limiting factor in the system performance. Therefore, a study of the motion noise of the airborne platform should be carried out first. Subsequently, the results of the two investigations will be presented and discussed.

## Study of the platform performance

Vector magnetometers suffer strongly from motion noise in airborne operation. Thus, the reduction of this noise in the target frequency range — from DC to $\sim 20$ Hz and to $\sim 100$ kHz for the $\mathrm{QMAG}^T$ and QAMT system — is of utmost importance. Two parallel tracks are followed to reduce motion noise: the post-processing of the SQUID data using the estimated attitude angles from the IMU and dGPS data for frequencies lower than $\sim 10$ Hz as well as the use of a towed bird with isolation/suspension of an inner platform to the shell for all frequencies above the corner at the lower end of the spectra. The latter also helps to improve the estimation of the attitude angles from the IMU sensor signals since it is also isolated from high frequency vibrations/motions (El-Sheimy and Youssef 2020).

The SQUIDs inside of the cryostat are placed at the center of gravity and rotation of the inner platform of the towed bird of generation 8, hereafter the so-called G8. The platform is well balanced at this point and held by a mechanical damping system against the shell by shock absorbing strings. They partly attenuate motion energy but mainly transfer high-frequency vibrations and motions into low-frequency signal range. Combined with an outer shell with a length of 3.65m, a diameter of 1.50m, and a mass of $\approx 300$ kg, the suspension allows for a low corner frequency (3Hz). More details on the subsequent development of the towed platforms can be found in Appendix 3.

**Comparative instrument** In order to draw a comparison to the state of the art instruments, an evaluation of the data quality against a towed bird without isolation and damping with SQUID-based FTMG instrument (Stolz 2015) and against an advanced induction coil bird (indicated as "WWU/BGR" hereafter) is performed. The induction coil bird is a joint development of the partners WWU and BGR in a German R&D project called DESMEX (Deep Electromagnetic Sounding for Mineral Exploration) and was successfully applied in several case studies (e.g., Smirnova et al. 2020; Steuer et al. 2020). Further details on the system can be found in Appendix 3.

All four platforms under comparison — WWU/BGR, G6wo, G7 and G8 — are shown in Fig. 5, for details refer to Appendix 3. Two performance measures were undertaken: the first one uses a direct comparison based on the

**Fig. 5** The towed platforms under comparison for their motion noise. Top left is the first platform for the SQUID-based instrument which is not used for comparison due to significantly higher noise figures
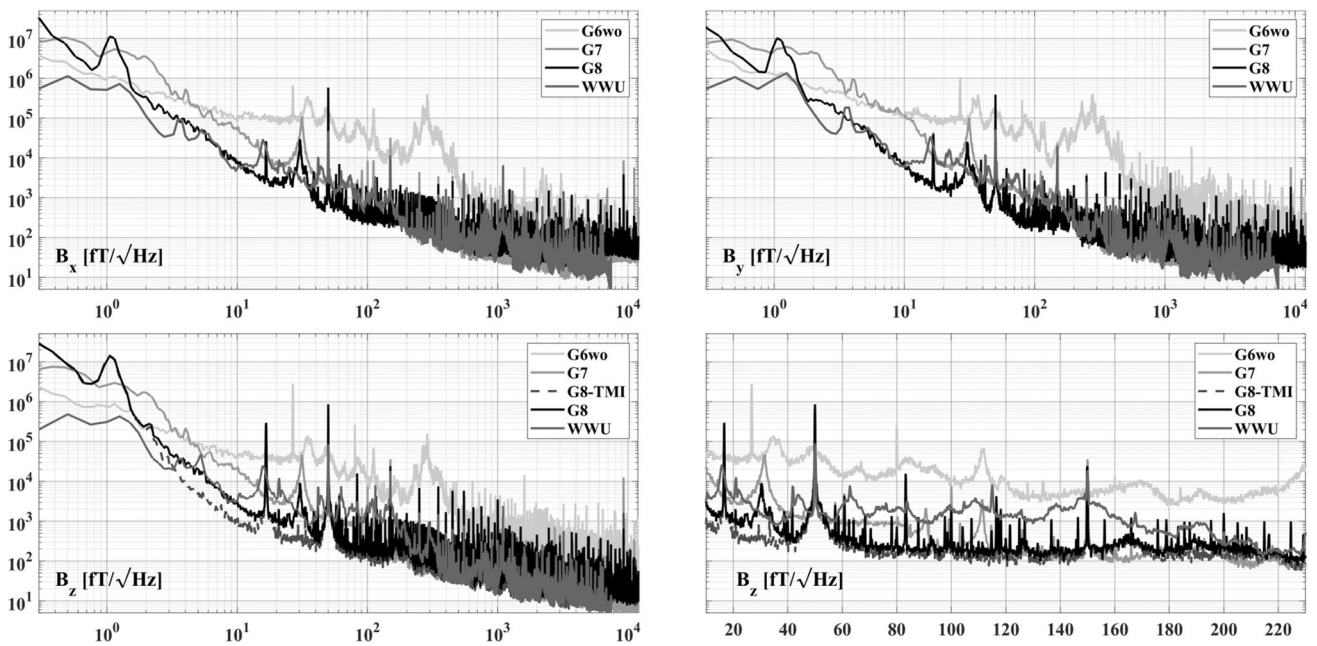


**Fig. 6** Noise comparison for the different towed platforms

magnetometer's signal spectra acquired along a straight line at high altitude with low turbulences. The second bases on transfer functions derived from the comparison flights during the semi-airborne EM study (more details in the "SAEM and AFMAG comparative study at Bad Grund, Germany" section). Data of two flights using WWU/BGR and G8

platforms, respectively, with identical flight lines and transmitter geometry were evaluated.

**Spectral comparison** The comparison of the spectra of all magnetic field vector components using the various platforms for the straight, long flight line at high altitude with

low turbulences is shown in Fig. 6. Those data are calibrated (Schiffler et al. 2014) and rotated into an Earth-fix Earth-centered coordinate system using the IMU processing (Schiffler 2017). The noise spectra are a composition of various influences such as geological and anthropogenic structures (e.g., $16\frac{2}{3}$Hz, 50Hz, and all harmonics), motion noise, platform signals, readout electronics and peripheral instrument contributions, and Helicopter-generated disturbances which lead to a wideband increase of the noise floor as well as a number of discrete peaks observable in the spectra in Fig. 6. It is obvious that the not suspended platform (G6wo) has signal levels which exceed the other platforms by a factor of more than 30 for a wide frequency range. Below 10Hz, the noise crosses over with the spectra of all suspended platforms. Suspension means to transform vibrations and motion from higher frequencies into the low-frequency band below a certain corner frequency. Below $\sim 300$Hz, the spectra from the WWU/BGR bird are about a factor of 10 higher than for the suspended SQUID platforms. In some frequency bands, this can be increased up to 50 (c.f. 110–140 Hz in the lower right panel of Fig. 6). Broad peaks at 16Hz and a few harmonics occur at frequencies < 100Hz. They might be related to tow rope vibrations. Intrinsic EM noise emitted by the IMU becomes evident at frequencies above about 300Hz. Only above $\sim 4$kHz the coil magnetometers achieve in the x- and y-direction the intrinsic induction coil noise floor of $\sim 30$fT$/\sqrt{\text{Hz}}$.

The initial suspended platform (G7) for the SQUID-based 3D-VM is for low frequencies worse than the new-generation platform (G8). Above $\sim 90$Hz, both platforms deliver comparable performances. Both platforms have a distinct wideband feature at frequencies $\sim 30$Hz which should thus be removed in a future optimization cycle. This spectral increase is however not observable in the calculated TMI. It is shown in the lower panels of Fig. 6. Thus, it is caused by a rotational motion which cannot be visible in the rotational invariant TMI, referring to the lower right-hand panel in Fig. 6. The optimized suspension lead to a decrease in amplitude for the G8 compared to G7 and also to a decrease in the frequency for the maximum.

The new suspended SQUID magnetometer bird (G8) has another feature at $\sim 1.05$Hz which is also visible in the TMI. This spectral peak points towards a translational motion. There are also a number of discrete peaks in the SQUID magnetometer spectra for the birds G7 and G8. However, the amplitudes are significantly lower than for the WWU/BGR bird and on top the amplitudes with the G7 bird are lower than for the G8 bird. This is understandable since the readout electronics is in the G7 bird not on the smaller-size suspended platform and has thus a larger distance to the SQUID system. However, the distance reduction and thus the slight increase of certain spectral noise components was

accepted in order to overcome the clear disadvantages of signal influences caused by the relative movement of SQUID unit and data acquisition system.

Even if the sensors have an intrinsic noise of < 1fT$/\sqrt{\text{Hz}}$ and about $7-10$fT$/\sqrt{\text{Hz}}$ measured in a shielded environment, the measured white system noise is currently $48, 32, 15$fT$/\sqrt{\text{Hz}}$ for the x-, y-, and z-channel, according to Fig. 6 respectively. The cause of this higher noise levels at high frequencies is under investigation. A further decrease of this noise level would provide a competitive advantage at very low frequencies. In a future optimization step, the lower corner frequency should be further reduced to well below 5Hz, the current value for the corner frequency is reported by Larnier et al. (2021).

## SAEM and AFMAG comparative study at Bad Grund, Germany

In this comparative study, the airborne SQUID-based QAMT instrument (installed in the G8 platform) and the WWU/BGR instrument underwent a demonstration for two geophysical methods — the semi-airborne EM method (SAEM) and AFMAG. Therefore, between August 23rd and August 25th, 2021, multiple flights in the old medieval mining area Oberharz (Germany) were conducted. Details on the Harz vein deposits can be found e.g. in Stedingk and Stoppel (1993) or Stedingk (2012) as well as references therein. The investigation area "Bad Grund" is located in the West Harz Basin. Mineralization is contained inside the calcitic Iberg reef. Around the site, lead, zinc, copper, and silver deposits up to a depth of 900m were exploited, and the operations were suspended in 1992. However, there are proven resources at depths greater than 1000m.

**Study conditions** The survey consisted of five flights. Four different grounded electric dipole transmitters (TX) of typically > 2.5km length were set up at different positions in order to provide a good spatial coverage of the area. For each TX, a survey grid centered at the transmitter position was flown by the QAMT instrument. A > 10A rectangular current waveform with 188ms period was injected providing a strong primary field of the TX. The flight path layout and transmitter locations are depicted in Fig. 7. One flight with a selected transmitter position and survey grid was repeated with the WWU/BGR induction coil bird, refer to Appendix 3. For the semi-overlapping grids, the measured magnetic field vector was processed and the transfer functions to the recorded transmitter current were estimated as described in Becken et al. (2020). For the two data sets, independent implementations were used as well as different choices of window lengths and spatial averaging lengths. Additionally, one AFMAG segment was flown.
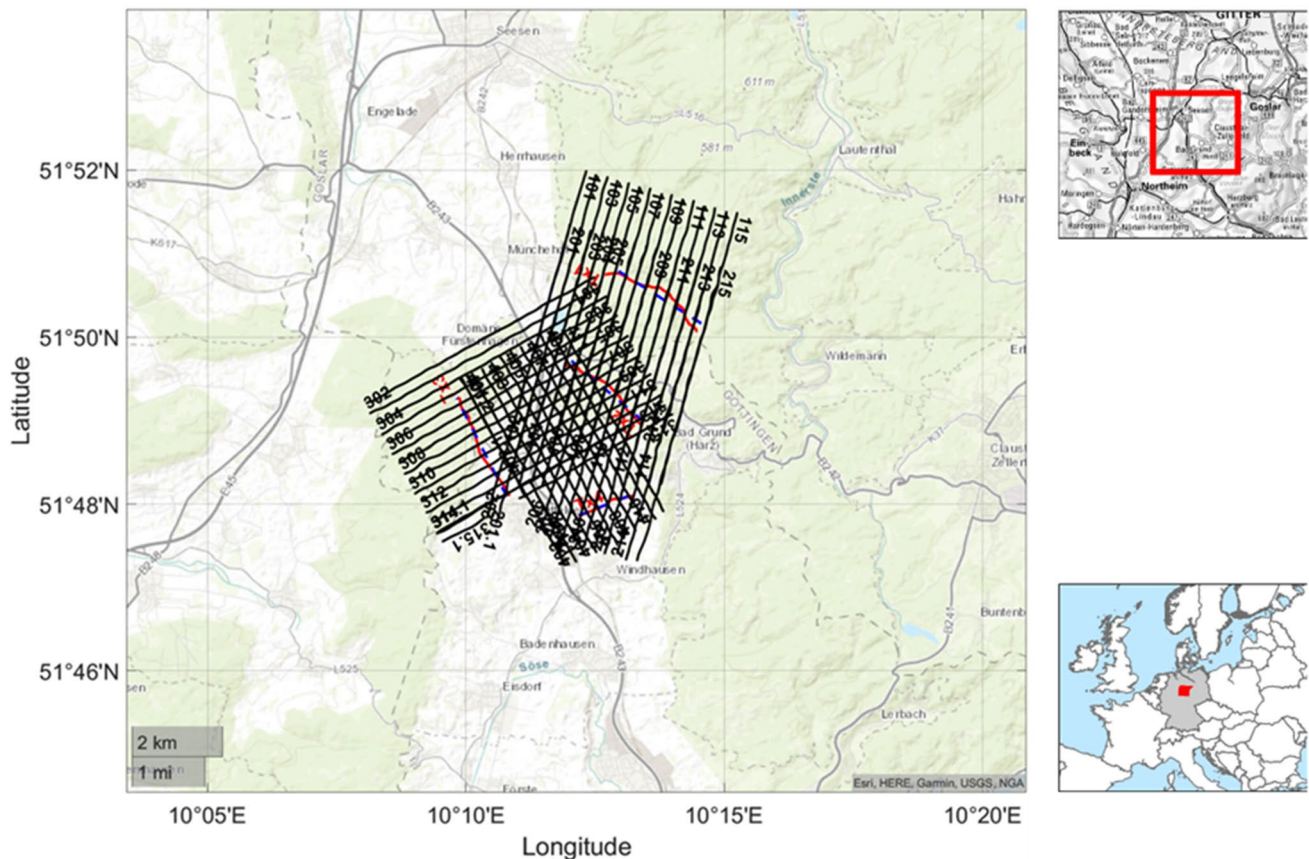
**Fig. 7** Layout of the SAEM survey in Bad Grund. The black lines denote the actual survey lines. Red structures indicate the positions of the according grounded dipole transmitters

**Results of the SAEM flights with the QAMT instrument** The maps of the vertical component of the magnetic transfer functions are depicted in Fig. 8 in terms of their real parts at a frequency of 90Hz. Data are shown for two independent flights using separated grounded transmitters. The real part includes the primary field and decays spatially with increasing distance from the TX. However, inductive effects in conductive features give rise to secondary fields and superpose on the primary field, which account for spatial asymmetry and give also rise to strong imaginary (out-of-phase) components. A linear feature running obliquely across the grids is consistently observable in both data sets. It is not a geological structure but correlates with technical infrastructure (pipeline), which couples to the primary field negatively and attenuates the diffusion of the field produced by the transmitter. Thus, the transfer function falls suddenly and stays diminished behind the pipeline. This example is therefore very challenging in terms of data interpretation in the presence of anthropogenic structures — a common problem in geophysical exploration in urban areas — and future R&D efforts must address such issues. However, the spatial smoothness and consistency of the data examples in

Fig. 8 illustrates the high quality of broad-band data that can be achieved with the new QS instrument for SAEM.

**Instrument comparison** The comparison was conducted for an area with a TX of 3km length and a $+/-20$A rectangular current waveform. Figure 9 shows the transfer function for two representative frequencies between vertical and horizontal magnetic flux density components, $B_z$ and $B_y$ (y-direction along the flight line), respectively, and the source current, estimated along a coincident flight line. The transmitter overflight has been truncated within 150m distance from the transmitter, and the phase of the vertical component, which exhibits a phase jump of 180° at the transmitter, has been shifted into common quadrants for clarity.

Transfer functions derived from the G8 platform show excellent quality in a broad frequency band (5 – 4000Hz). Amplitude and phase curves of horizontal and vertical components are smooth even for large receiver-transmitter distances of up to 3km and for both the vertical and the horizontal components, respectively. Both platforms perform equally well at intermediate and high frequencies
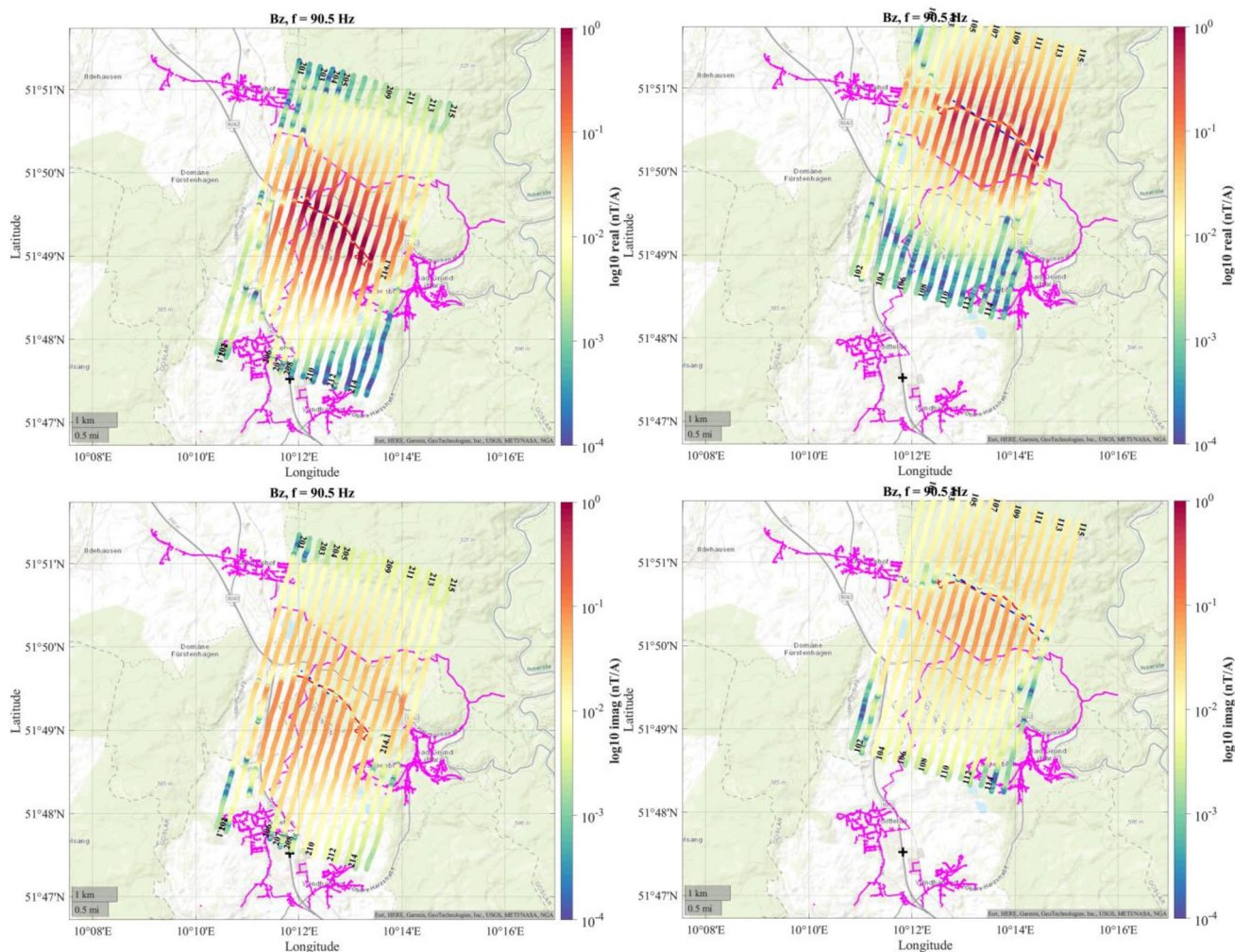
**Fig. 8** Estimated transfer functions for a representative frequency of 90.5Hz and two transmitter positions for the Bad Grund case study. The amplitude at this frequency is plotted on the according position of the receiver on the flight line. The red and blue dashed lines denote the actual transmitter geometry and the strike direction of the transmitter, respectively. The transfer functions are color-coded on a logarithmic scale. The spatial consistency suggests good data quality across all shown flight lines. The wide range of the logarithmic scale shows the large signal to noise ratio in this data set. Transfer functions are attenuated for locations when crossing anthropogenic structures. For example, the gas pipelines in the survey area are shown here (in magenta)

(see 90.5Hz and 724Hz) but data quality retrieved from the WWU/BGR bird significantly diminishes at lower frequency bands (see example data at 5.3Hz).

At low frequencies, data quality is mainly affected by motion noise, causing phase fluctuations and larger estimation uncertainties. Motion noise significantly reduces data quality of the WWU/BGR platform along the whole flight line at frequencies below ∼ 100Hz. At frequencies < 50Hz, it is enhanced on the inner sensor platform due to the eigenfrequency of the damping system at 10–20 Hz. For frequencies 50Hz < f < 100Hz, the WWU/BGR bird still only has a reduced damping effect. Furthermore, the WWU/BGR bird includes a 1-Hz high-pass filter to suppress pendulum-motion-induced voltages which would exceed the input range of the analogue to digital converter (ADC).

Therefore, the sensitivity of the WWU/BGR bird is reduced at frequencies below ∼ 10Hz. G8 data, in turn, are seemingly less distorted by motion noise at the lowermost frequency (5.3Hz) depicted in Fig. 9, and motion noise is confined to the northern part of the profile section (−3 to −2km) where the platforms were towed across rough topography. Transfer functions derived from the G8 platform in the southern part are spatially very consistent and only have a small standard error even at the lowermost frequency, suggesting reliable data quality which is in parts due to a superior damping system.

Especially the amplitude of the vertical component attenuates rapidly with increasing receiver-transmitter distance at high frequencies. Data quality of both platforms reduces at amplitudes < $10^{-3}$ nT/A. Discrepancies between horizontal

**Fig. 9** Comparison of semi-airborne EM transfer function determined from recordings with the G8 and the WWU/BGR instruments: **a** horizontal magnetic transfer function, **b** vertical magnetic transfer functions. Three representative frequencies are shown. The data are from a helicopter measurement near Bad Grund, Harz mountains (Germany) that were conducted in 2021. Data from the transmitter overflight within 150**m** distance to the transmitter have been truncated; the phase of the vertical component is shifted into a common quadrant. The transfer functions derived from the G8 recordings show less noise (refer to error bars), especially in the phase, compared to the data determined from the WWU/BGR instrument
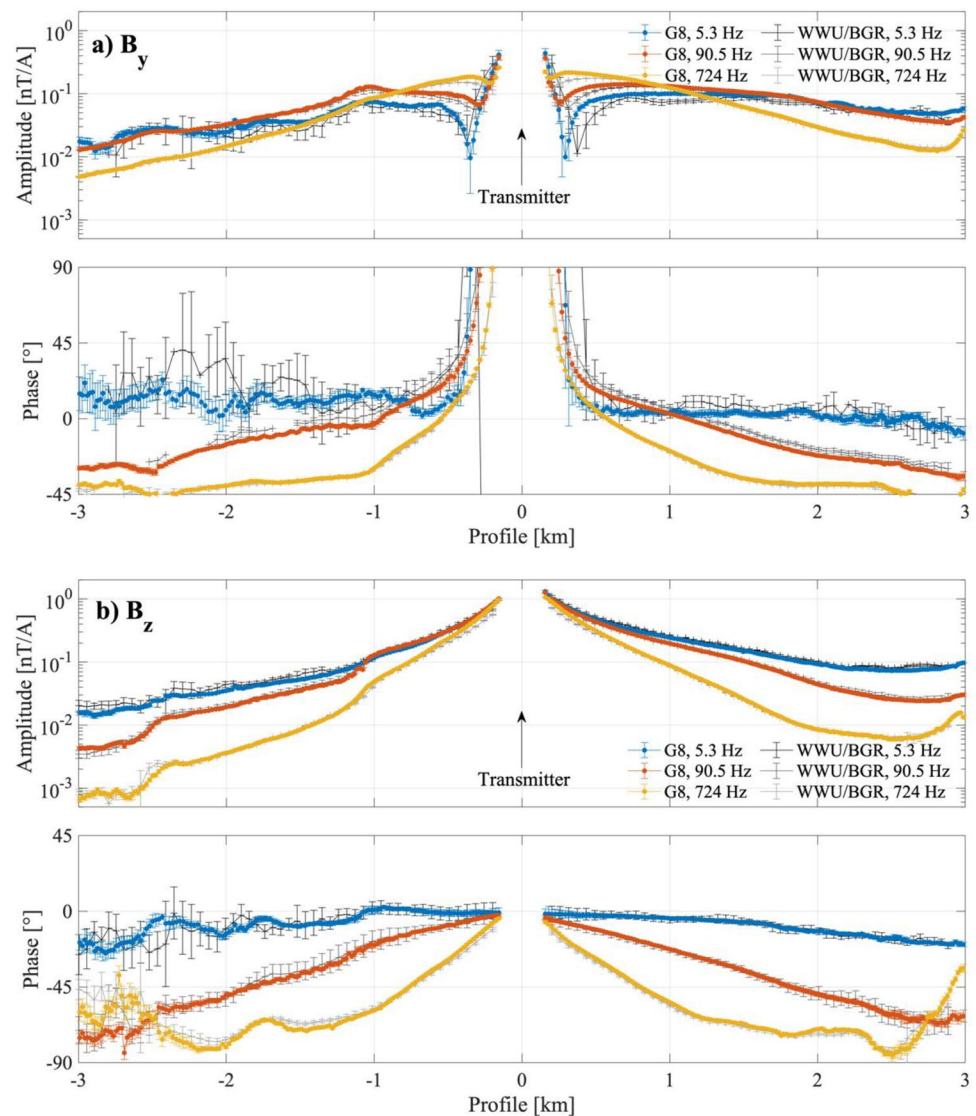


field amplitudes and phases derived from the G8 and WWU/BGR instruments might result from inaccurate reconstruction of the corresponding field components in a North-East-Down (NED) coordinate system.

## Demonstration in Ludvika, Sweden

Several case studies were already undertaken and reported in the past for FTMG demonstrations, such as (1) in the Bushveld Igneous Complex in the Republic of South Africa (RSA), e.g., Rompel (2009), Schiffler et al. (2017), FitzGerald et al. (2009); (2) for greenfield exploration in RSA for kimberlites by Letts and Stolz (2017); (3) within European R&D projects, e.g., HYPGEO in the Spanish pyrite belt (Meyer et al. 2017); (4) in the INFACT project at Sakatti prospect (INFACT consortium 2018); (5) in the INFLUINS (integrated fluid dynamics in sedimentary basins) project for targets of various geological characters

within the Thuringian basin (Queitsch 2016; Queitsch et al. 2019); and (6) recent fully commercial large-size surveys in Canada (example by Stolz et al. 2021a). For the QAMT system, only one test has been performed so far. Thus, the aim of the case study is to evaluate the performance specifications[3] of airborne SQUID-based instrument demonstrators within the R&D project AMTEG (Advanced Magnetic Tensor Gradiometer) over the test site close to Ludvika in Southern/Central Sweden. The main part of the project tasks was to deliver a magnetization and an electrical conductivity model from the qualitatively high-grade iron ore deposits Blötberget and Håksberg. The according geological setting

---

[3] For the FTMG and QAMT instrument, the robust operation as well as magnetic gradient and magnetic field resolution in combination with bandwidth and *SNR* in survey operation were to be evaluated here, respectively.
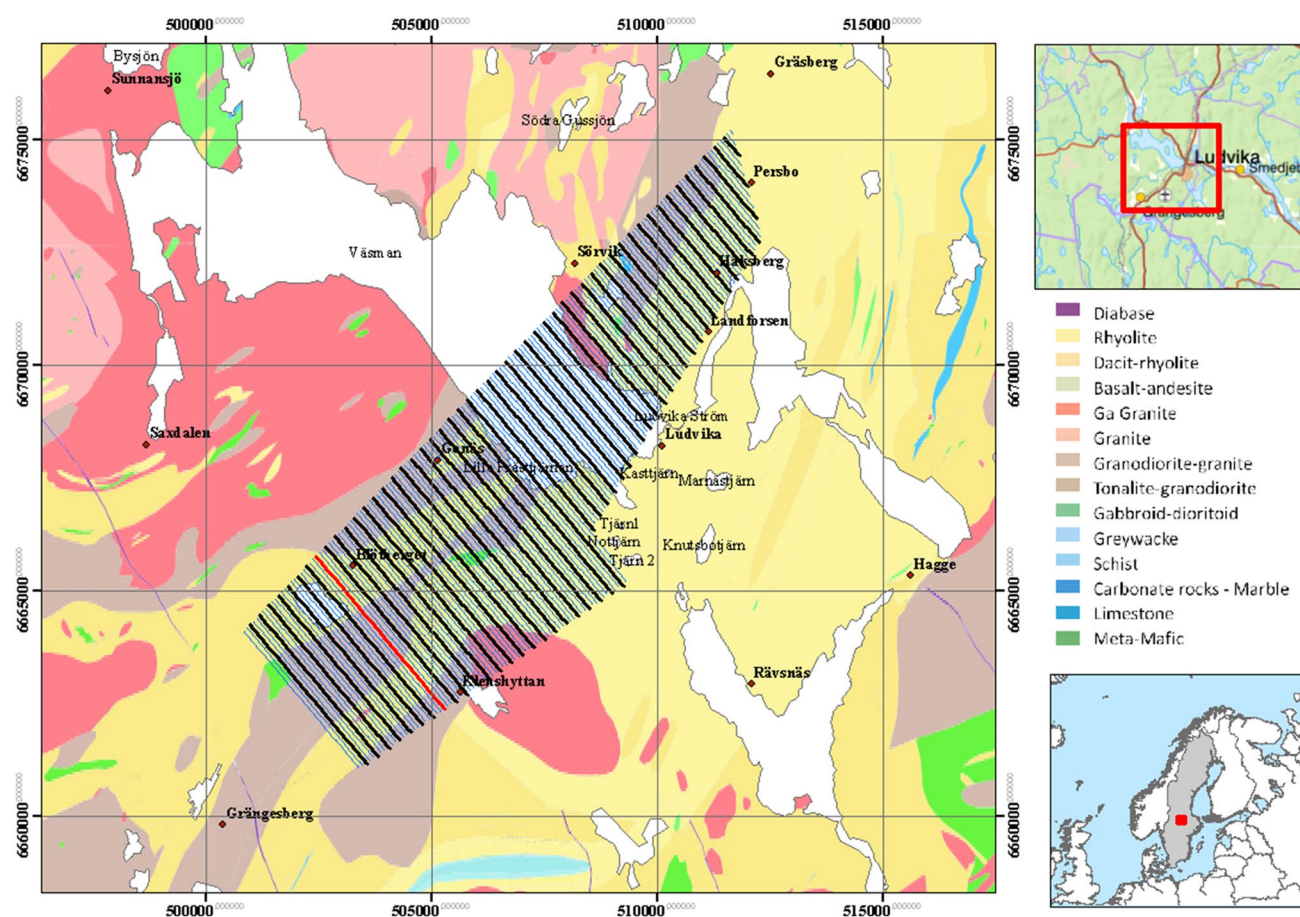
**Fig. 10** Simplified geological map showing the major lithological units of the Blötberget survey area. The profile lines for the FTMG grid and the AFMAG survey are represented by the thin blue and the bold black lines, respectively. The red line denotes the results of the section shown in Figs. 16 and 17

and former geophysical measurements of these sites are described by Bastani et al. (2019) in detail.

The measurement area, c.f. Figure 10, is located in the ore district Bergslagen and stretches from Grängesberg in the South over the mining area Blötberget, along Ludvika over the Väsman lake towards Håksberg in the North, where metamorphosed volcano-sedimentary rocks of Paleoproterozoic age (1.85–1.80 Ga) are dominating the host rock. Types of mineralization encompass banded iron formations, skarns, and apatite-rich deposits. The ore body under detailed investigation in AMTEG represents an apatite-rich deposit. This type of mineralization contributes to approx. 40% of the total iron ore production in this area. The expected mineralization is traceable down to at least 800–850 m in depth with an inclination of ~45–50° towards southeast direction.

On August 2nd and August 3rd 2021, the electromagnetic measurements were performed encompassing 51 profile lines with a line-to-line spacing of 300m which is suitable for the AFMAG method. In order to obtain a high-definition geomagnetic data set, flights with the QMAG$^T$ demonstrator were performed on August 3rd and August 4th with a much denser grid of 100m profile line spacing (155 lines). The flight line direction was from south-east to north-west. Anthropogenic noise sources in the area include power lines, electrified railways, high-frequency transmitters, and a lot of dwellings which contribute to a number of magnetic anomalies in the FTMG data and affect the AMT noise level negatively. The topography to be taken into account for inversion and interpretation is moderate.

### FTMG data set

Using the processing scheme described by Schiffler (2017), the magnetic gradient tensor component maps in Fig. 11 were produced from the FTMG data. They image the internal structure of the magnetic anomalies produced by the iron ore bodies with high definition but contain also a number of anomalous signals of anthropogenic disturbances. Unfortunately, the anthropogenic anomalies by railway lines and dwellings have a good spatial correlation with the
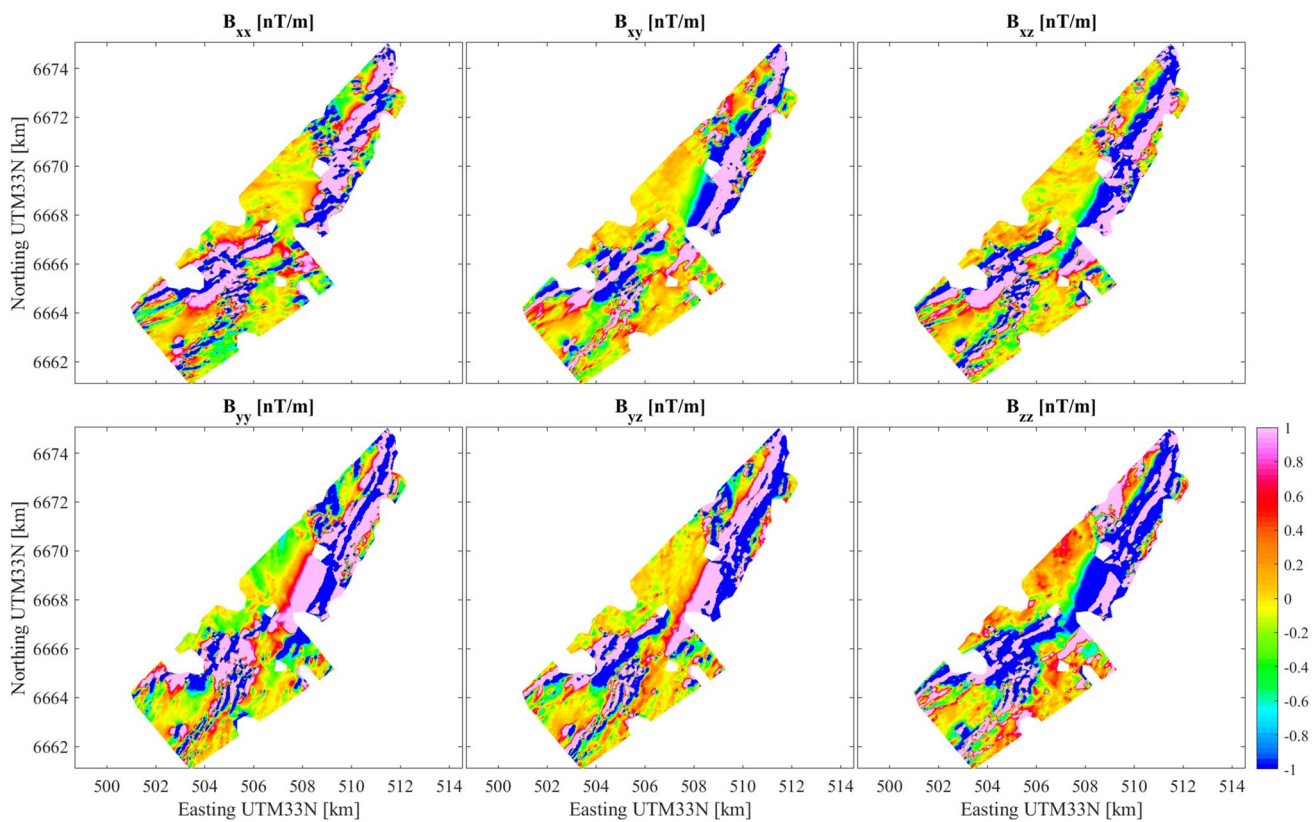
**Fig. 11** Tensor component maps

magnetized rock structures which prevents replacement of these anomalies from the data with interpolated values from the surrounding area. However, the interpretation of the inverted 3D model of the magnetization vector takes care of it. For subsequent commercial operation of the instrument, a high-resolution DEM will be acquired and incorporated in the inversion for structures located on the surface only and subtraction of these predicted anomalies.

Subsequently, a full magnetization vector inversion (MVI) was performed using the code developed in Schiffler (2017) based on the regularized reweighted conjugate gradient (RRCG) algorithm presented in Zhdanov (2002). The sub-surface space was discretized into a mesh of $458 \times 656 \times 160$ voxels, with each having a volume of $25 \times 25 \times 12.5 \text{m}^3$. The vertical cell size is half of the horizontal dimension to gain higher vertical resolution. In order to take the topography into account, voxels above the intersection of a digital elevation model with a resolution of $\sim 92$m in north–south direction and $\sim 46$m in east–west direction are removed from the model space. The geological plausibility of the model of the magnetized mineral body was enhanced by using a minimum support (Portniaguine and Zhdanov 1999) regularization producing more compact anomalies. Furthermore, the magnetization vector is represented by spherical coordinates (inclination, declination, and

intensity of the magnetization). Reflecting Cella and Fedi (2012), the depth weighting parameter $\beta$ proposed in Li and Oldenburg (1996) was set to $\beta = 0.8$. The result of the MVI using all five independent magnetic gradient tensor components is depicted in the upper panel of Fig. 12.

In a second step, a MVI jointly using FTMG and total magnetic field intensity (TMI, Fig. 13) derived from the 3D-VM data by $B = \left| \vec{B} \right| = \left( B_x^2 + B_y^2 + B_z^2 \right)^{1/2}$ was performed. For this inversion, also a depth weighting parameter of $\beta = 0.8$ was used.

The TMI inversion seems to balance the FTMG inversion in the near-surface cells. The result of the joint MVI is shown in the lower panel of Fig. 12. For the pure FTMG MVI, the data misfit was reduced within 25 iterations from 7.3 down to 4.6 nT/m$_{\text{RMS}}$. The inversion stopped since the decrease of misfit compared to the iteration before was only 0.2%. Contrarily, the data misfit for the joint FTMG and TMI MVI was reduced within 25 iterations from 1766.7 nT$_{\text{RMS}}$ (TMI part) down to 429.2 nT$_{\text{RMS}}$ which is a better fit than the FTMG inversion. Within the joint inversion, the misfit of the magnetic gradient tensor was reduced to 6.3 nT/m$_{\text{RMS}}$. Furthermore, a forward calculation of the TMI with the pure FTMG MVI model shows a misfit of 972.3 nT$_{\text{RMS}}$. The misfit progress of the inversion is presented in Fig. 14 and to

**Fig. 12** MVI inversion models: pure FTMG inversion and joint FTMG and TMI (derived from 3D-VM) in the top and lower panel, respectively. The model from the pure FTMG inversion shows near-surface focused magnetizations reflecting mostly anthropogenic sources and tends to reproduce the orebody-related magnetizations to a bit deeper extent. Contrarily the modeled anomaly underneath the Väsman lake I produced more confined within the pure FTMG inversion than the combination with the TMI
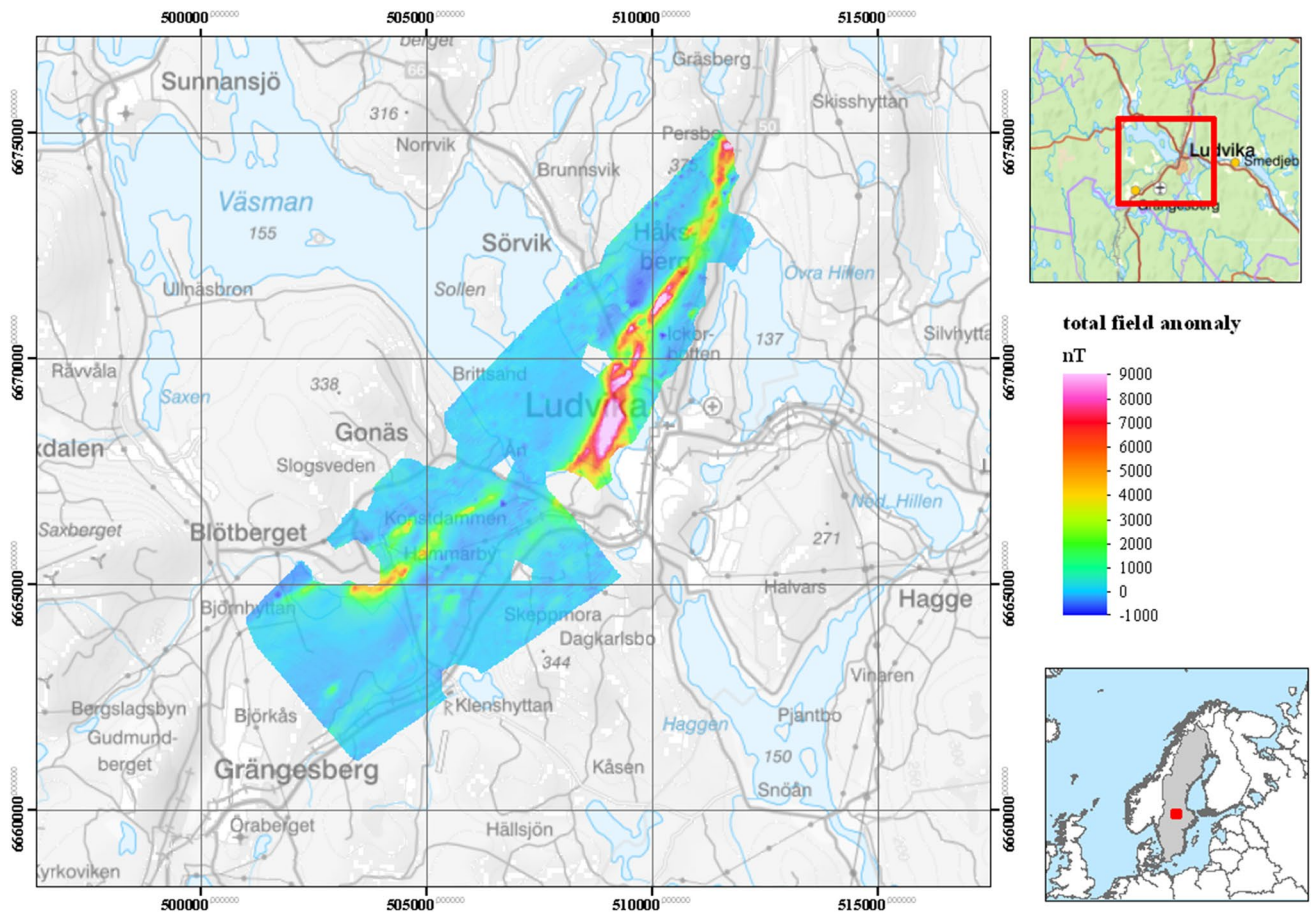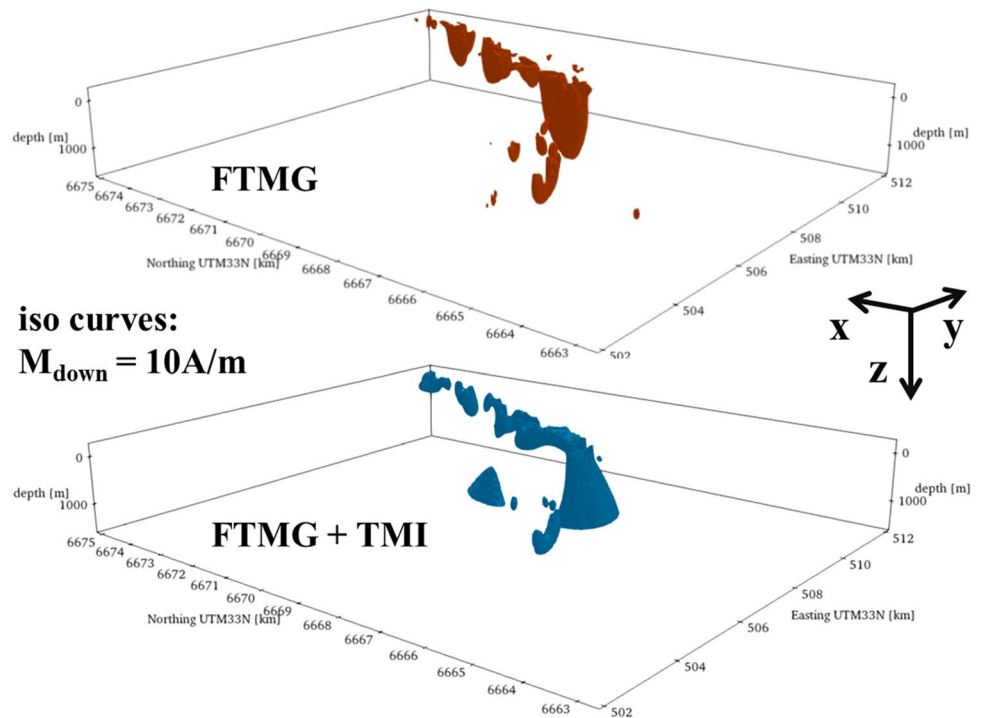


**Fig. 13** Map of the anomalies of the total magnetic intensity derived from the measurements with the SQUID-based 3D vector magnetometer for the Blötberget survey area
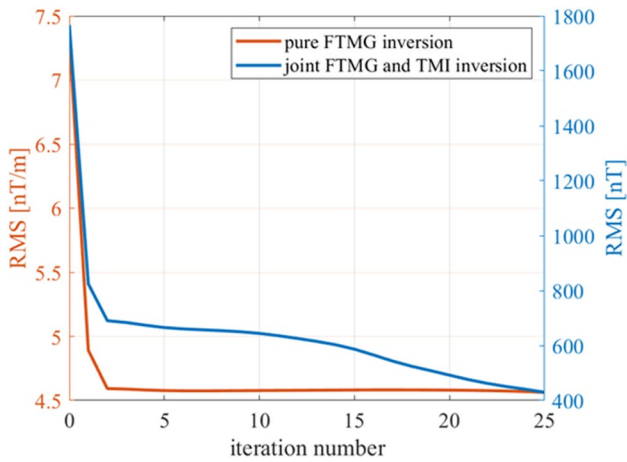
**Fig. 14** Misfit during the iteration progress of the MVI using the joint inversion of TMI and FTMG in blue and pure FTMG inversion in red, respectively

obeys the law $1/r^4$ whereas the corresponding law for the TMI is $1/r^3$. Thus, the pure FTMG inversion is more affected by the quality of modeling of the near-surface voxels and the presence of near-surface disturbances. As the anthropogenic structures are located on the Earth, the resolution of topography is the primary anomaly source. Here, a SRTM image is used as DEM; a combination with high-precision altimeter measurements would enhance the modeling quality. Unfortunately, the high-resolution altimeter failed operation during the particular survey flight. In contrast, it has been shown that a combination of FTMG and TMI survey, joint inversion, and interpretation is beneficial for magnetic modeling in mineral exploration.

## AFMAG data set

The AFMAG data contained in the airborne and ground-based 3D-VM measurements were processed in frequency
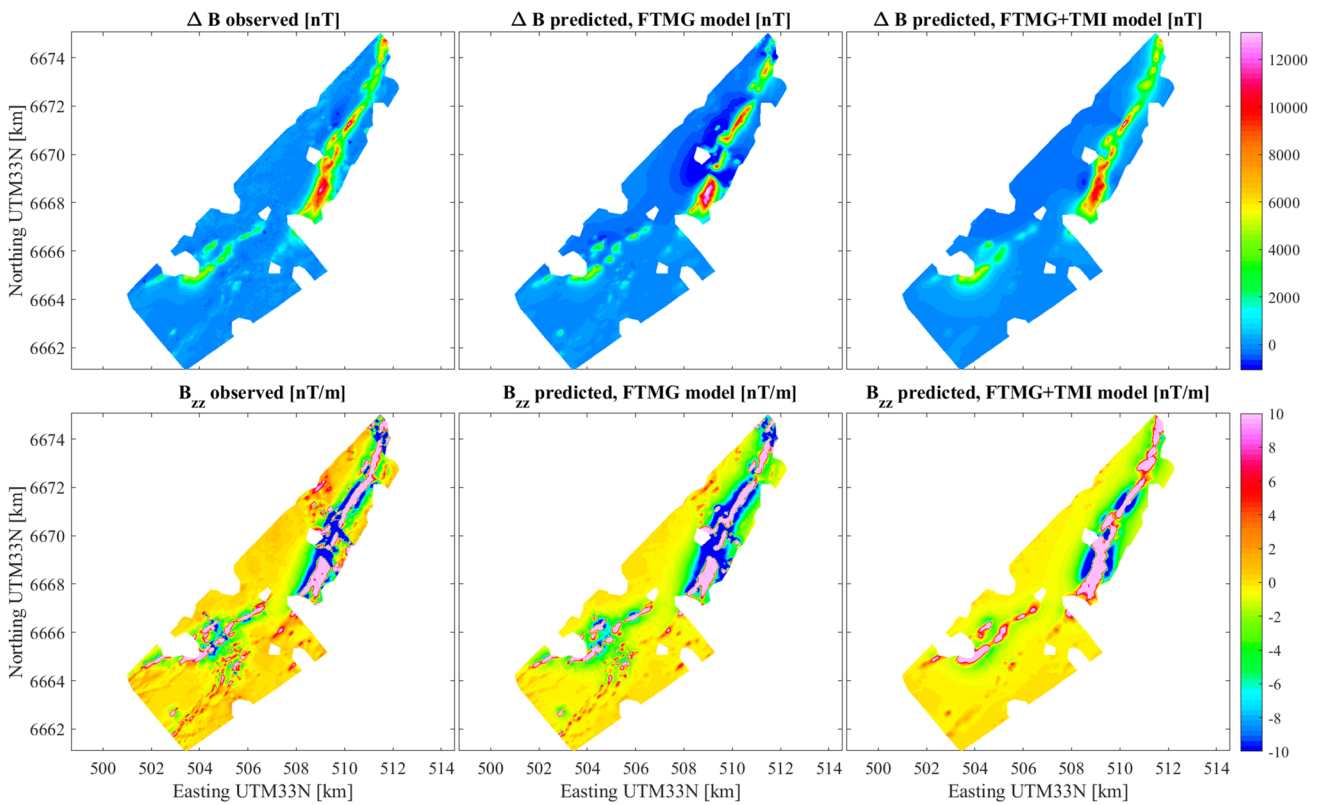


**Fig. 15** Comparison between the observed and predicted total field anomaly and magnetic gradient tensor component $B_{zz}$ showing a good explanation of the measured anomalies by both models. The

pure FTMG inversion focuses towards a better modeling result for the magnetic gradient tensor data while the joint inversion drives the modeling result towards the details of the TMI data, respectively

show the quality of both inversions, the observed and predicted data are compared in Fig. 15 proving that the anomalies are well explained by both models. For explanation of the different misfits achieved, the following has to be considered: The decay behavior of the magnetic gradient tensor

space in order to obtain the distribution of vertical magnetic transfer function (VMTF or tipper, see definition in Becken et al. 2008). The in-flight tipper component was inverted for six frequencies in the range between 30 and 300 Hz with the

**Fig. 16** Electrical resistivity model of Line 10,080 from the AFMAG data in Ludvika survey reflecting a section of the resistivity of the ore body with approx. 300**Ωm** in the center of the anomaly inside a host rock with a resistivity of 5000**Ωm**
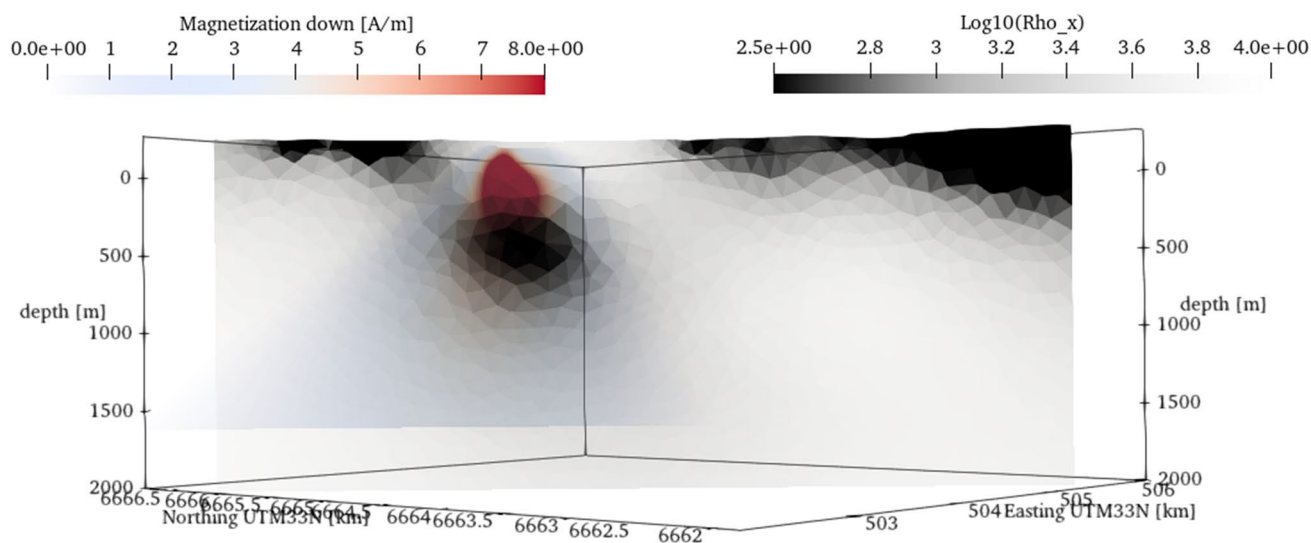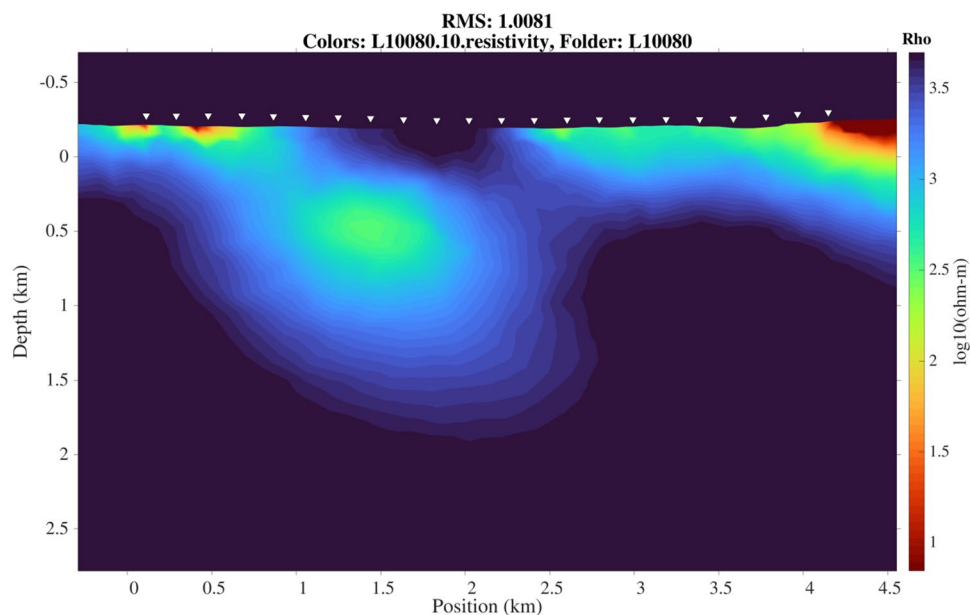


**Fig. 17** Overlay of the models for magnetization (downward direction) and resistivity for the Ludvika case study

2.5D modeling and inversion program MARE2DEM (Key 2016). Therein, the topographic profile was extracted for each profile line. Afterwards, the inversion mesh was discretized with fine resolution into triangles with an edge length of in maximum 200m down to a depth range of 2km. The air and the further sub-surface model space were discretized as coarse as possible with ∼ 5km edge length. For the inversion of the electrical conductivity within this framework, a Gauss–Newton algorithm and Occam's razor regularization were engaged to produce a smooth resistivity model. Fig. 16 shows the inversion result of a particular flight line intersecting the area covered by the borehole measurements presented in Maries et al. (2017) which will be discussed

against the MVI and AFMAG inversion results in the next paragraph. The inversion finished after 10 iterations achieving the target misfit of 1.0 down from an initial misfit of 1.83.

### Results of the inversion

Two different models of FTMG and AFMAG data inversion are overlain in Fig. 17 and will be firstly interpreted geometrically before comparing with the borehole data published in Maries et al. (2017): Located west of Ludvika, the largest anomaly is produced due to the ore body underneath the Väsman lake. Stretching to the Håksberg

in the North, the strike angle and the depth of the ore body and its resulting anomaly seem to be consistent. However, the magnetic anomalies are intersected by lots of anthropogenic influence which is mirrored by small near-surface magnetization anomalies in the 3D sub-surface model. In the Blötberget area, a strong magnetic high is observable caused by a well-known iron-oxide body with > 50% magnetite content (Bastani et al. 2019). In comparison to the magnetization anomaly close to Håksberg, the modeled body herein appears to be smaller than the one depicted by Bastani et al. (2019) which is reflected by the more complex structure of the magnetic gradient tensor. The geometry of the modeled resistivity anomaly approximatively fits laterally to the MVI model. However, the combined use of FTMG and TMI data and more focused regularization of the MVI indicates the shallower part of the ore bodies whereas the AFMAG data and the smoothing stabilizer for the inversion highlight their deeper part.

The borehole susceptibility and electrical resistivity logs show (cf. Figure 4 in Maries et al. 2017) within the mineralization depth range of 350–450 m underneath the surface a susceptibility anomaly of up to $\approx 10^4$cgs and a resistivity anomaly of von $\approx 500\Omega$m inside non-anomalous values of $< 10^3$cgs and $\approx 3000–10,000\Omega$m, respectively. The anomaly sections depicted in Fig. 17 show anomalous magnetization values of $> 8$ A/m and electrical resistivity values of $\approx 300\Omega$m within a matrix of $\approx 5000\Omega$m which is in very good accordance with the reported borehole values. Within an ambient magnetic field of $51,600$nT, a susceptibility anomaly of $10^4$cgs would produce a magnetization amplitude of $5.16$A/m. A likely remanent part could contribute to the magnetization retrieved by MVI. The decomposition of induced and remanent magnetization is described in Queitsch et al. (2019) and comprises the calculation of the projection of the full magnetization vector onto the ambient earth's magnetic field direction $\overrightarrow{e_{B_0}} = \overrightarrow{B_o}/\left|\overrightarrow{B_o}\right|$ which reflects the induced part

$$M_i = \overrightarrow{M} \bullet \overrightarrow{B_o} \Big/ \left|\overrightarrow{B_o}\right| = \overrightarrow{M} \bullet \overrightarrow{e_{B_0}}$$

The remanent contribution is then derived by the subtraction $M_r = \left|\overrightarrow{M} - M_i \bullet \overrightarrow{e_{B_0}}\right|$. As no remanence measurements were reported in Maries et al. (2017) and Bastani et al. (2019) which only shows susceptibility models, a ground truth is not possible. Using this projection, a remanent part of approx. 0.1 A/m is estimated (Koenigsberger ratio of $Q \approx 0.01$) but this estimate neglects any remanent part parallel to the Earth's magnetic field direction.

## Ground-based TEM with SQUIDs

Transient EM (or time domain EM, pulse EM, etc.), herein abbreviated as TEM, was developed as a geophysical technique mainly in the 1950s (Harthill 1976; Nabighian and Macnae 1991). It implements a large-size transmitter coil (TX) with a generator driving a constant current through it. When the primary field of the TX is abruptly switched off, a system of eddy currents is generated in the sub-surface which diffuses to the depth and the sides. As the diffusion velocity depends on the conductivity of the sub-surface structures, the decay curve of the secondary magnetic field is thus a diagnostic tool to derive the conductivity-depth profile at a measurement site.

### State of the art

The state of the art sensors for TEM are still induction coils. However, the measurement of magnetic field components vs. its time derivatives provides a number of advantages such as the sensitivity for late time responses, the lower dynamic range required, and an improved target vs. overburden response ratio which were discussed by a number of publications (McCracken et al. 1986; Smith and Annan 1998; Osmond et al. 2002; Macnae 2006; LeRoux and Macnae 2007; Asten and Duncan 2012; Rochlitz et al. 2018; Wolfgram and Thomson 2018). Since the advent of the SQUID-based receivers in the 1990s, they developed as a mature technology being today in full industrial use. Examples for the various SQUID-based TEM instruments are given by Stolz et al. (2021b).

In Jena, two species of SQUID-based TEM receivers were developed: JESSY DEEP LTS and HTS. The first requires cooling with lHe which is more demanding. On the other hand, it provides very good magnetic field resolution of $< 2$fT/$\sqrt{\text{Hz}}$ (Chwala et al. 2013), wide bandwidth, and slew rate as well as good stability during magnetically unshielded operation. Depending on the external conditions and the amplitude of the TX signal to be recorded, a low (ML2 SQUIDs) or a high (ML7 SQUIDs) sensitive triplet can be used. This instrument is also used as a base station for the airborne SQUID-based EM instruments. The second receiver species uses the HTS SQUIDs introduced earlier in this work. It has lower field resolution and slew rate but is simpler to be operated in the field. The parameter sets for the JESSY DEEP instruments are provided by Stolz et al. (2021b).

Today, more than 20 instruments from Jena are in continuous worldwide operation. There have been a great number of case studies. However, they are often not disclosed or published by the clients. A number of them
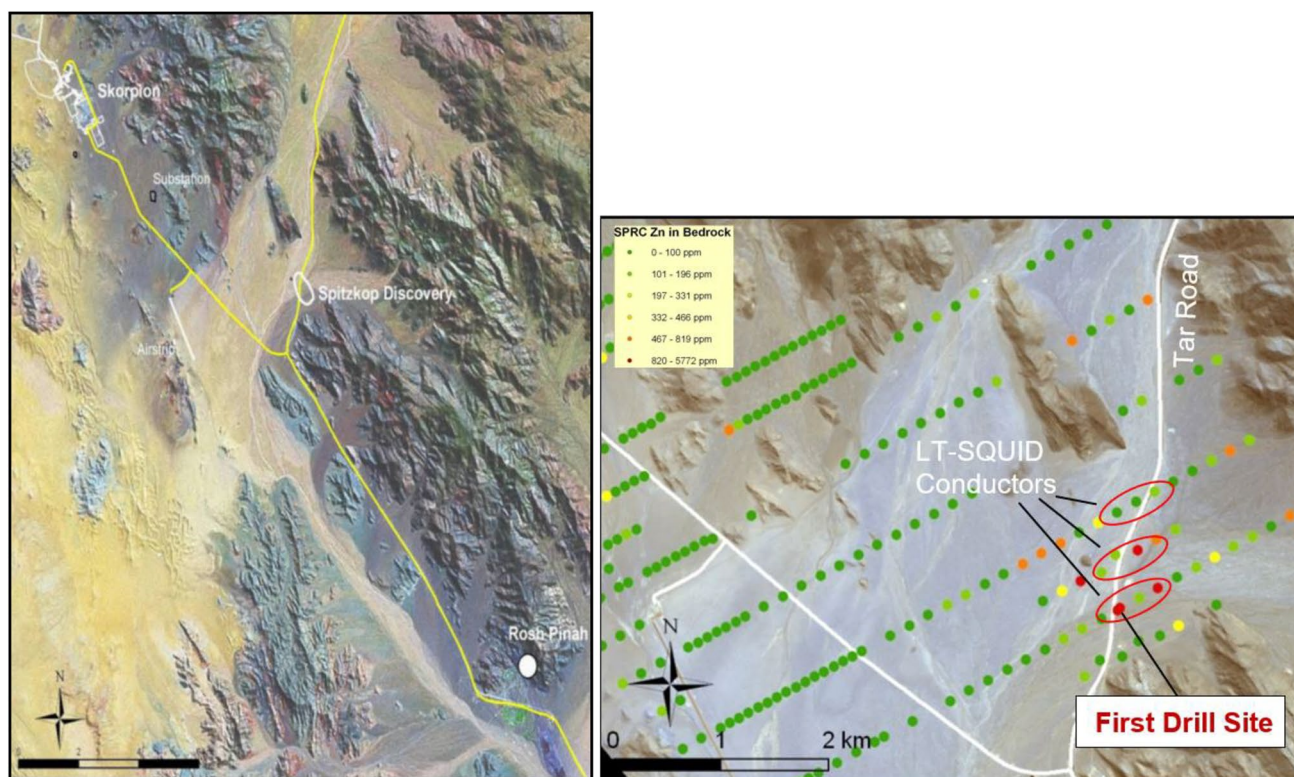
**Fig. 18** Left and right are the location of Gergarub within the overburden-filled Spitzkop Valley and of the LTS SQUID conductor in relation to the RC Zn results, respectively

could be found in LeRoux and Macnae (2007), Terblanche (2008), Smit and LeRoux (2009), Webb and Corscadden (2009), Selfe (2009), Woods (2010), Rochlitz et al. (2018), etc.

## Case study: Gergarub, Namibia

Gergarub (Spitzkop) is a Neoproterozoic Pb–Zn (Ag) VMS deposit, hosted by the Gariep Belt in south-western Namibia. The deposit was discovered by Anglo American in 2008 in what was, up to then, considered a mature brownfields mining district. Two operating mines, Skorpion and Rosh Pinah, are located within less than 15 km from Gergarub; and both mines have been discovered more than 30 years earlier. The fact that Gergarub was discovered much later than the existing mines in the district can be ascribed to the application of a modern exploration methodology and its location in a large overburden-filled valley (Spitzkop Valley, Fig. 18). Any potential outcrop expression was concealed by up to 100 m of transported colluvial cover and the deposit therefore entirely "blind."

The Spitzkop Valley was selected as a high-priority structural target in 2005. By June 2007, a significant anomaly was detected in several reverse circulation (RC) holes on two lines in the south-western part the Spitzkop Valley. A maximum of 0.35% Zn and 0.50% Pb was found in weathered bedrock of hole SPRC319, very near the bedrock-overburden interface. Trough infill drilling the bedrock anomaly was found to occupy an area of approximately 1km × 1km (Fig. 18).

Lacking any indication of a sub-outcropping orebody, ground-based moving-loop electromagnetics (MLEM) was chosen to follow-up on the geochemical anomaly. The intention was to find a possible conductor, which could aid in siting an appropriate deeper follow-up hole. The LTS SQUID system was deployed to the project area to be used as the TEM sensor. Three lines of MLEM were conducted over the anomaly, following the same spacing of 400m and direction of the original drill lines. A single-turn transmitter loop of 200m × 200m was used and a station spacing of 100m applied.

Each of the lines showed a strong and well-defined conductor. On each line, the conductor appeared to have a near flat-lying horizontal geometry. The decision was taken to drill test the conductor that coincided with the best geochemical anomaly, which was located on the southernmost line. Forward modeling was carried out with the Maxwell plate modeling software version 4.1 and resulted in a near flat lying plate (1000m × 700m) with a conductance of 800S. EMAX (Fullagar Geophysics Pty Ltd.) and EMFlow

**Fig. 19** RC holes plotted over CDI generated in EMFLow from LTS SQUID MLEM data. Red bar plots next to RC holes display relative Zn concentrations down the hole
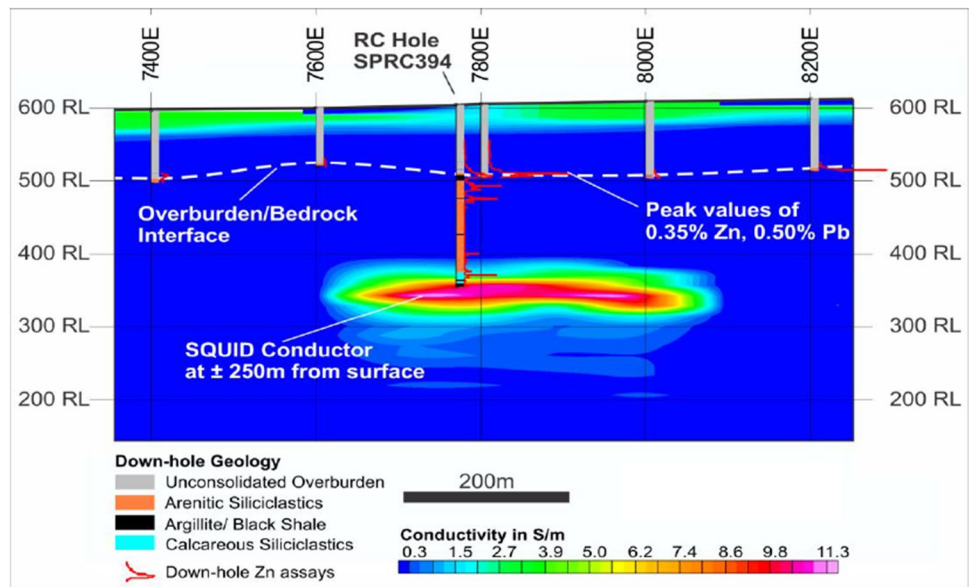


(Macnae and Xiong 1998) conductivity-depth image (CDI) algorithms were used to generate the conductivity-depth images.

The first deep RC attempt to drill the conductor failed and the hole was just short of intersecting the expected target (Fig. 19).

In order to establish whether the conductor had indeed been intersected by the RC drill hole, a down-hole electromagnetic (DHEM) survey was initiated, using an Atlantis 3-component B-field probe. The survey indicated that the main conductor had not been intersected and was located very close to the bottom of the RC hole. In early June 2008, a diamond rig was used to deepen the hole. On the 6th of June 2008, only 4m below the bottom of the RC hole, the diamond drill rig intersected massive and semi-massive sulfide mineralization from 254m. The diamond drill tail to the RC holes was extended to 359.5m. However, in the 60m of core that was recovered, two separate ore horizons were intersected. The upper horizon included 4 m with 9.8% Zn, 3.4% Pb, and 71ppm Ag. The lower horizon contained 7m at 8.6% Zn, 3.2% Pb, and 43ppm Ag. Both intersections proved to be typical representations in width and grade compared to subsequent intersections of the ore horizons (Duggan 2010).

Subsequent to the discovery Airborne EM (AEM), both Fixed Wing and Helicopter EM were flown over the area and the calculated Tau[4] grid results in relation to the LTS SQUID data with the ore body outline overlain are shown in Fig. 20.

---

[4] The specific time (tau — $\tau$) is the measure of the speed of decay of the EM response. It indicates the presence of conductive structures. Tau is estimated by fitting the TEM decays to a function $e^{-\tau/t}$.

## Summary and outlook

New quantum sensors will provide an impact in mineral exploration with their specific features and performance specifications. In this work, we discussed the state of the art of quantum sensors — namely the use of a quantum system, quantum properties, or quantum phenomena to perform a measurement of a physical quantity — which have potential to be used in geophysical exploration with magnetic and electromagnetic methods based on published sensors, instruments, and demonstrations.

Thereafter, we introduce our research on SQUID-based quantum sensing instruments which are emerging, on the cusp, and already in routine use for geophysical investigations: The QAMT instrument is a new airborne SQUID-based vector magnetometer with wide bandwidth and huge dynamic range (*SNR*) aimed for the use in AFMAG or the semi-airborne EM method (DESMEX). One example for AFMAG measurements at the Ludvika investigation site in Sweden is presented which demonstrates the low-noise figure in a broad frequency range and has thus great potential to get a new tool for exploring passive EM signals of the Earth magnetic field.

The secondly introduced system turned in the past few years into commercial operation — the QMAG[T] full tensor magnetic gradiometer. It enhances the imaging quality of magnetic anomalies in spatial and magnetic sense, provides remanence indication, and already has proven a great track report in commercial exploration operations. This instrument is still limited by the readout electronics. Within the R&D project AMTEG, a new large *SNR* readout was demonstrated and will soon be implemented into the new QMAG[T] system generation.
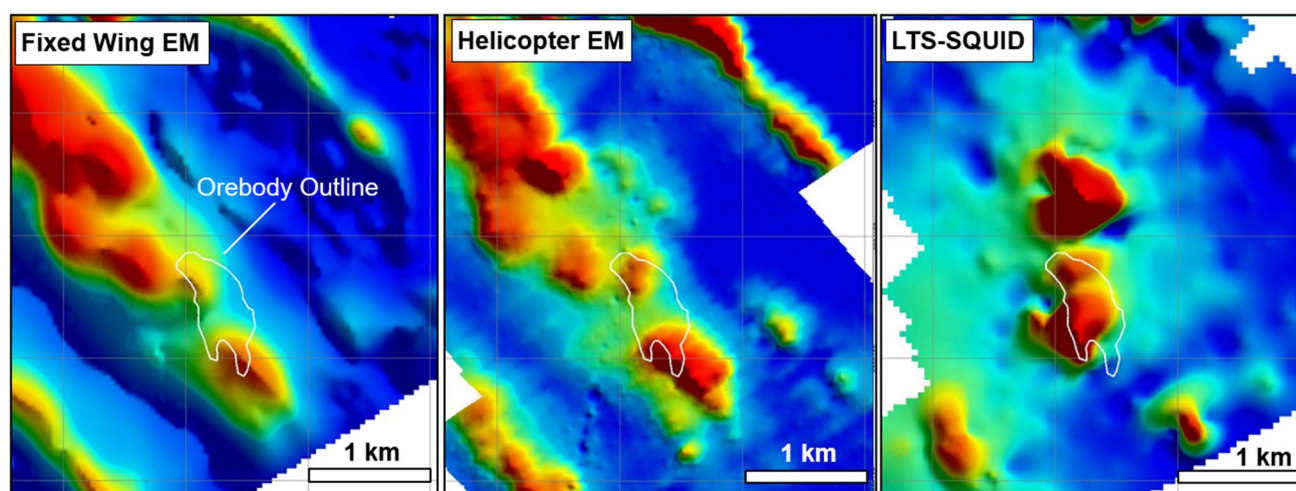
**Fig. 20** Qualitative comparison of the Tau grids of AEM systems and the LTS SQUID over Gergarub VMS deposit. The LTS-SQUID data range approximately from 0.7 to 100 ms from dark blue to dark red colors. The scaling for the airborne measurements was not released by the client. The LTS SQUID Tau grid highlights the significantly higher Tau values associated with massive sulfides and the Zn mineralization well in relation to the airborne data, which largely outlines only the phyllitic host rock

In the ground-based TEM method, SQUID-based 3D receivers became already state of the art exploiting their advantage to record directly the components of the Earth magnetic field rather than their time derivatives. These instruments have a great success record over the past 10 years in industry. The use of these instruments open up new applications as base stations for MT/QAMT measurements or for magnetically measured induced polarization (MIP, Chubak and Woods 2013). Another future option for ground-based TEM receivers with SQUID is to implement the flux counting readout to overcome the noise limit of the electronics and to record strong magnetic field amplitudes of new high-power transmitters.

Quantum sensing will in the mid-term future offer new instruments for exploration which hold great promises for advanced exploration tools in future:

### OPMs

- New versions from R&D will allow for better noise specifications than commercially available OPMs and will thus allow for new airborne tools also on unmanned platforms,
- In the long term, new OPMs with vectorial sensitivity will evolve; open up the space of 3D vector magnetometry or their use in TEM,

### SQUID-based quantum sensing tools

- The technologies introduced herein allow for multimodal airborne platforms without increasing size and mass for the joint acquisition of FTMG, 3D-VM, AFMAG, and AMT data; the implementation of a scalar-type OPM would improve the calibration of the SQUID magnetometer readings significantly,
- Reducing the system noise and enhancing the slew rate of the new SQUID instruments with huge *DR* further would enable their use in advanced airborne FTMG and TEM instruments to gain the same advantages over induction coils as demonstrated already for ground-based TEM receivers.

## Appendix 1. The two quantum revolutions

One has to distinguish clearly between the first and second quantum revolution and accordingly two generations of the QTs. The first quantum revolution shaped the twentieth century and the second one is expected to do it with the twenty-first century.

The first generation (QT1.0) uses quantum phenomena such as the Josephson effects for superconducting circuits to enable new functionalities. Typical examples are transistors, lasers and masers, atomic clocks, and magnetic resonance tomography which created a remarkable impact for society. The second generation of the QTs (QT2.0) has again the potential of a revolutionary evolution for society. They are based on new or previously unexploited quantum effects and should make use of the entanglement of individual quantum states to enable new R&D fields such as computation and simulation, communication and enhanced imaging, quantum sensing, and metrology as well as enabling technologies. The QT2.0 facilitate the use of various technological platforms like semi- or superconducting elements, ion traps,

photonic or topological circuits, quantum dots, color-centers like nitrogen vacancies, and NMR and atom spectroscopically technologies (Amundson et al. 2019).

## Appendix 2. Magnetometer specification

One important feature of any magnetometer is the *magnetic field resolution* which relates directly to the *sensor's noise* floor $B_n = \sqrt{S_B}$ in units of $\mathrm{T_{RMS}}/\sqrt{\mathrm{Hz}}$[5]. Therein, $S_B$ is the noise spectral density taken from the calculated Fourier spectra in the region of frequency independent noise. In order to draw the reader's or user's attention to the following facts: in academia mostly, only the *intrinsic white noise* floor is given. This has two issues: Depending on the signal frequency range of interest, one has also to account for the colored noise (increasing noise levels in the spectra for low frequencies described by $S_B \sim f^{-\alpha}$) and random walk for the sensor under investigation. On top for some quantum sensors often only the theoretical noise floor is provided such as for OPMs often the shot-noise limited level. However, for real applications, the total system noise including the digitization and recording of the signals is required for the user. This level is often much higher than the intrinsic noise. Other important parameters are the *cross-talk* and especially the *linearity* of the response. In case of any use of reference sensors, a high value for the latter is required. Also important is the *slew rate* (the ability to track fast signals with high amplitude changes) of the sensor. These parameters are often not provided by academia or instrument providers. Finally, the lower the noise floor, the more important the *dynamic range* (distance between noise floor and maximum trackable signal amplitude — definition for all magnetometer types; similar to definition of signal to noise ratio (*SNR*) of of the used analogue to digital converters (ADCs): $DR = 20\mathrm{dB} \bullet \log_{10}(B_{\mathrm{max,pp}}/B_{\mathrm{noise,pp}})$. Since in geophysical applications the sensors may not be used inside of well magnetically shielded environment, the *DR* may achieve very high values which are not realizable with today's semiconductor components especially for vector-type sensors having one sensitive axis. Let us assume a sensitive magnetometer with noise of $5\mathrm{fT}/\sqrt{\mathrm{Hz}}$ and a horizontal sensitive axis rotating in Germany around the vertical axis. This will lead to a magnetic field change of about $B_{\mathrm{max,pp}} \approx 40\mathrm{\mu T}$ which results in a *DR* of 149.8dB.[6] An ideal 24-bit ADC would only provide a *SNR* ($\approx DR$) of 145dB. As a consequence, for all QSs

with exceptionally low noise, ways of tracking signals with huge *DR* are required.

Let us briefly review the latest developments for conventional magnetic field sensors with respect to the magnetic field resolution: There are still improvements in conventional-type induction coil sensors, e.g., Poliakov et al. (2017). Besides those, in the past decade, new induction coil sensors were developed, so-called B field coils (Macnae 2012) which allow for the measurement of the magnetic field with a noise floor of $\sim 10\mathrm{fT}/\sqrt{\mathrm{Hz}}$ but at the expense of significant low-frequency noise. Significant improvements have also been achieved for FGMs: new core materials and geometries were investigated which led to a lower noise floor. As outstanding example, Vetoshko et al. (2016) achieved $< 90\mathrm{fT}/\sqrt{\mathrm{Hz}}$ with yttrium garnets in a magnetically shielded environment. It is not known how these sensors behave in the Earth's magnetic field.

## Appendix 3. The airborne platforms under comparison

### SQUID-based platform

In the past two decades, various platforms were developed and implemented for operation of the SQUID-based FTMG instrument. Starting with vertical birds (generation 1 up to 3; gen. 2 depicted in Stolz et al. 2006), new streamlined platforms with a drag tail were developed (generation 4 and 5; gen. 4 depicted in Stolz 2015). Most of the case studies cited herein have been undertaken with the platform generation 6 (referring herein to "G6wo" without isolation/damping; more details in Fig. 3.4 in Queitsch 2016), a light weight (130kg) construction with rigid connection of the SQUID instrument, and all other peripheral components inside. The latest two generations implement a suspended internal sensor platform. Generation 7 (hereafter called "G7") has almost the same outer dimensions like the "G6wo" platform. Therein, only the SQUID instrument, a reference fluxgate, and the IMU are mounted on the suspended platform. All other devices are rigidly assembled on the outer shell. The newest platform called "G8" has an increased size of the inner platform to implement all components. Thus, the outer shell has a larger dimension and the mass increased to $\sim 300\mathrm{kg}$ to enlarge the moment of inertia. Also, the suspension measures are improved in order to reduce the lower corner frequency of the motion noise in the 3D-VM data.

### Comparative platform with induction coil sensors

For the comparative platform, an outer shell of a DIGHEM-V platform (indicated by "WWU/BGR" hereafter) was used. It was internally re-designed to fit three induction coil

---

[5]   RMS are root-mean-square values from the Fourier spectra calculation. This index will be omitted in here as everywhere else in literature.

[6]   For a 1-kHz signal bandwidth, the noise floor is transformed to $5\mathrm{fT}/\sqrt{\mathrm{Hz}} \bullet \sqrt{1\mathrm{kHz}} \bullet 8 \approx 1.3\mathrm{pT}$ using a Crest factor of 8. Thus, the example gives $SNR = 20\mathrm{dB} \bullet \log_{10}(40\mathrm{\mu T}/1.3\mathrm{pT}) = 149.8\mathrm{dB}$.

sensors, a fluxgate magnetometer, a data logger, a conventional OPM, an IMU, and a Wifi router. The induction coils are of type MFS11e (Metronix GmbH). Their signals are digitized at sampling frequency of 16, 384Hz by a 24-bit data logger of type ADU-07e also by Metronix GmbH. The coils have an internal feedback system resulting in a flat response function and a sensitivity of 134mV/nT in the frequency range ~ 0.1–3 kHz. Their intrinsic noise level is $\sim 30\text{fT}/\sqrt{\text{Hz}}$ at 10Hz. More details on this instrument are provided in Becken et al. (2020). Motion noise due to vibrations becomes evident in the induction coil data below frequencies of ~ 200Hz, in parts due to vibrations of the tow ropes and the skirt. Due to limited space in the DIGHEM-V shell, the WWU/BGR bird uses a damping foam material instead of a suspension system in order to suppress high frequent vibrations. The sensor platform is decoupled from the outer shell by Sylomer® SR11 foam and each coil is decoupled from the inner platform by Sylomer® SR18 foam to avoid internal high-frequency vibration noise emitted by the IMU. A comparison to an undamped platform shows effective damping at frequencies > 50Hz. The eigenfrequency of the damping system lies between 10 and 20Hz as indicated by an increased noise level. Current efforts are directed towards improved mechanical suspensions of internal sensor platforms.

## Appendix 4. Available SQUID technologies

For the magnetic field readings at one hand, highly sensitive LTS SQUID magnetometers are used. They are based on Josephson junctions made of Nb-AlO$_X$-Nb realized in a multi-loop configuration (Drung 1997). The junctions are sub-micrometer-sized structures for very low-noise performance (Anders et al. 2009). By scaling the area, the pickup area and the magnetic field resolution of the SQUIDs can be increased. The 2-mm (ML2a) and 7-mm (ML7)-diameter LTS SQUIDs published by (Schmelz et al. 2012) are implemented in the instruments introduced herein. They have typically an intrinsic white noise floor of $\sim 3.5\text{fT}/\sqrt{\text{Hz}}$ and $\sim 0.7\text{fT}/\sqrt{\text{Hz}}$, respectively. Their HTS counterparts are used in the ground-based instruments. They are realized in YBaCuO$_{7-x}$ structures with step-edge Josephson junctions (Kaczmarek et al. 2018). For the FTMG instrument, LTS SQUID–based intrinsic gradiometers are used. They are planar-type and of first-order with a chip size of $6\text{cm} \times 2\text{cm}$. The intrinsic gradient noise is well below $50\text{fT}/\left(\text{m} \bullet \sqrt{\text{Hz}}\right)$, refer to Fig. 2. The structure and its performance are discussed by Stolz (2015) and in detail a comparison to all R&D on SQUID gradiometers by Stolz et al. (2020).

**Abbreviations** 3D-VM: 3D vector magnetometer; ADC: Analogue to digital converter; AEM: Airborne electromagnetic; AFMAG: Audiofrequency magnetics; AMT: Audiofrequency magnetotellurics; CDI: Conductivity-depth image; dGPS: Differential Global Positioning System; DHEM: Down-hole electromagnetic method; DR: Dynamic range; EM: Electromagnetic; FD: Frequency domain; FDEM: Frequency domain EM method; FGM: Fluxgate magnetometer; FTMG: Full tensor magnetic gradiometry; HTS: High-temperature superconductivity (typically operated in lN$_2$ at 77K); IMU: Inertial measurement unit; IP: Induced polarization; JESSY DEEP: Jena SQUID system for deep earth exploration; LTS: Low-temperature superconductivity (typically operated in lHe at 4.2K); MLEM: Ground-based moving-loop electromagnetics; MT: Magnetotellurics; MVI: Magnetization vector inversion; NED: North, east, down coordinates; NVCD: Nitrogen vacancy centers in diamond; OPM: Optically pumped magnetometer; QAMT : Quantum sensor–based system for audiofrequency magnetotellurics; QS: Quantum sensor; QT: Quantum technologies; RC: Reverse circulation; SAEM: Semi-airborne EM methods; SGG: Superconducting gravity gradiometry; SNR: Signal to noise ratio; SQUID: Superconducting quantum interference device; TD: Time domain; TEM: Transient electromagnetics or time domain EM method; TMI: Total magnetic field intensity; TX: Transmitter; VMS: Volcanogenic massive sulfide

## Declarations

**Ethics approval and consent to participate** Not applicable.

**Consent for publication** All authors agree to publish the submitted file.

**Conflict of interest** The authors declare no competing interests.

## References

Amundson J, Sexton-Kennedy E, Forti A, Betev L, Litmaath M, Smirnova O, Hristov P (2019) Quantum computing. EPJ Web of Conf 214:09010. https://doi.org/10.1051/epjconf/2019214090 10

Anders S, Schmelz M, Fritzsch L, Stolz R, Zakosarenko V, Schoenau T, Meyer HG (2009) Sub-micrometer-sized, cross-type Nb-AlOx-Nb tunnel junctions with low parasitic capacitance. Supercond Sci Technol 22:64012. https://doi.org/10.1088/0953-2048/22/6/064012

Asten MW, Duncan AC (2012) The quantitative advantages of using B-field sensors in time-domain EM measurement for mineral exploration and unexploded ordnance search. Geophysics 77:WB137–WB148. https://doi.org/10.1190/geo2011-0385.1

Bal M, Deng C, Orgiazzi J, Ong FR, Lupascu A (2012) Ultrasensitive magnetic field detection using a single artificial atom. Nat Commun 3:1324. https://doi.org/10.1038/ncomms2332

Bartington instruments Ltd (2020) Mag-03 three-axis magnetic field sensors. http://www.bartington.com/mag-03-three-axis-magnetic-field-sensor.html. Accessed 4 March 2020

Bastani M, Sadeghi M, Malehmir A, Luth S, Marsden P (2019) 3D magnetic susceptibility model of a deep iron-oxide apatite- bearing orebody incorporating borehole data in Blötberget, Sweden. Extended Abstracts - 16th SAGA Biennial Conference and Exhibition 2019:1–4

Becken M, Ritter O, Burkhardt H (2008) Mode separation of magnetotelluric responses in three-dimensional environments. Geophys J Int 172:67–86. https://doi.org/10.1111/j.1365-246X.2007.03612.x

Becken M, Nittinger CG, Smirnova M, Steuer A, Martin T, Petersen H, Meyer U, Mörbe W, Yogeshwar P, Tezkan B, Matzander U, Friedrichs B, Rochlitz R, Günther T, Schiffler M, Stolz R (2020) DESMEX: a novel system development for semi-airborne electromagnetic exploration. Geophysics 85:E253–E267. https://doi.org/10.1190/GEO2019-0336.1

Budker D, Jackson Kimball DF (eds) (2013) Optical magnetometry. Cambridge University Press, Cambridge

Cella F, Fedi M (2012) Inversion of potential field data using the structural index as weighting function rate decay. Geophys Prospect 60:313–336. https://doi.org/10.1111/j.1365-2478.2011.00974.x

Chai YQ, Zhang M, Wei LF (2022) Sensitive detection of local magnetic field changes with atomic interferometry by using superconducting meissner effects

Christensen AN, Dransfield MH (2002) Airborne vector magnetometry over banded iron-formations. In: SEG Technical Program Expanded Abstracts 2002. Society of Exploration Geophysicists, Houston, pp 13–16

Chubak G, Woods D (2013) Magnetic induced polarization - using new technology for greater detection capability of deep and elusive mineralization. ASEG Extended Abstracts 2013:1–4. https://doi.org/10.1071/ASEG2013ab312

Chwala A, Kingman J, Stolz R, Schmelz M, Zakosarenko V, Linzen S, Bauer F, Starkloff M, Meyer M, Meyer HG (2013) Noise characterization of highly sensitive SQUID magnetometer systems in unshielded environments. Supercond Sci Technol 26::35017. https://doi.org/10.1088/0953-2048/26/3/035017

Clarke J, Braginski AI (eds) (2004) The SQUID Handbook. Wiley-VCH Verlag GmbH & Co. KGaA, Weinheim

Cohen Y, Jadeja K, Sula S, Venturelli M, Deans C, Marmugi L, Renzoni F (2019) A cold atom radio-frequency magnetometer. Appl Phys Lett 114:073505. https://doi.org/10.1063/1.5084004

Commercial OPM providers (2020) Scintrex Ltd. 2017 CS-3 cesium magnetometer: high resolution magnetics. http://scintrexltd.com/dat/content/CS-3.pdf, Geometrics G-824A https://geometrics.com/wp-content/uploads/2018/10/G-824ASpecSheetPROOF072017.pdf, Twinleaf microSAM: https://twinleaf.com/scalar/microSAM/, QuSpin QTFM, Total Field Magnetometer http://quspin.com/wp-content/uploads/2016/09/QMAG-TF-Spec-Sheet.pdf. Accessed 1 Mar 2022

Danilin S, Lebedev AV, Vepsäläinen A, Lesovik GB, Blatter G, Paraoanu GS (2018) Quantum-enhanced magnetometry by phase estimation algorithms with a single artificial atom. npj Quantum Inf 4:339. https://doi.org/10.1038/s41534-018-0078-y

Drung D (1997) Improved dc SQUID read-out electronics with low 1/f noise preamplifier. Rev Sci Instrum 68:4066–4074. https://doi.org/10.1063/1.1148348

Drung D, Mück M (2004) SQUID Electronics. In: Clarke J, Braginski AI (eds) The SQUID Handbook. Wiley-VCH Verlag GmbH & Co. KGaA, Weinheim, pp 127–170

Duggan SP (2010) Gergarub mineral resource estimate. Report compiled by Z-star Mineral Resource Consultants for Skorpion Mining Company (Pty) Ltd, p 34

El-Sheimy N, Youssef A (2020) Inertial sensors technologies for navigation applications: state of the art and future trends. Sat Nav 1:42. https://doi.org/10.1186/s43020-019-0001-5

FitzGerald DJ, Holstein H (2006) Innovative data processing methods for gradient airborne geophysical data sets. Lead Edge 25:87–94. https://doi.org/10.1190/1.2164762

FitzGerald DJ, Argast D, Holstein H, Paterson NR (2009) Full tensor magnetic gradiometry processing and interpretation developments

Fullagar PK, Fallon NG (1997) Geophysics in metalliferous mines for ore body delineation and rock mass characterisation. Exploration 1997:573–584

GEM Systems Inc. (2020) Short review of optically pumped scalar magnetometers

Gerginov V, Pomponio M, Knappe S (2020) Scalar magnetometry below 100 fT/Hz 1/2 in a microfabricated cell. IEEE Sens J 20:12684–12690. https://doi.org/10.1109/JSEN.2020.3002193

Grant F, West GF (1965) Interpretation theory in applied geophysics. International series in the Earth sciences. Mc Graw-Hill, New York

Grosz A, Haji-Sheikh MJ, Mukhopadhyay SC (eds) (2017) High sensitivity magnetometers. Springer International Publishing, Cham

Harthill N (1976) Time-domain electromagnetic sounding. IEEE Trans Geosci Electron 14:256–260. https://doi.org/10.1109/TGE.1976.294435

Hinze WJ, von Frese R, Saad AH (2013) Gravity and magnetic exploration: principles, practices, and applications. Cambridge University Press, Cambridge

Hogg S (2004) Practicalities, pitfalls and new developments in airborne magnetic gradiometry. First Break 59–65. https://doi.org/10.3997/1365-2397.22.7.25952

INFACT consortium (2018) INFACT IN BRIEF: FACTSHEET #1. http://www.supracon.com/files/online/NormaleNanoskalige/INFACT_factsheets3.pdf. Accessed 19 Feb 2020

Jaklevic R, Lambe J, Silver A, Mercereau J (1964) Quantum interference effects in Josephson tunneling. Phys Rev Lett 12:159–160. https://doi.org/10.1103/PhysRevLett.12.159

Janosek M, Butta M, Dressler M, Saunderson E, Novotny D, Fourie C (2020) 1-pT Noise fluxgate magnetometer for geomagnetic measurements and unshielded magnetocardiography. IEEE Trans Instrum Meas 69:2552–2560. https://doi.org/10.1109/TIM.2019.2949205

Kaczmarek LL, IJsselsteijn R, Zakosarenko V, Chwala A, Meyer H, Meyer M, Stolz R (2018) Advanced HTS dc SQUIDs with step-edge Josephson junctions for geophysical applications. IEEE Trans Appl Supercond 28:1–5. https://doi.org/10.1109/TASC.2018.2820056

Kaminski V, Viezzoli A (2017) Modeling induced polarization effects in helicopter time-domain electromagnetic data: field case studies. Geophysics 82(2):B49–B61. https://doi.org/10.1190/geo2016-0103.1

Key K (2016) MARE2DEM: A 2-D inversion code for controlled-source electromagnetic and magnetotelluric data. Geophys J Int 207:571–588. https://doi.org/10.1093/gji/ggw290

Koschorreck M, Napolitano M, Dubost B, Mitchell MW (2011) High resolution magnetic vector-field imaging with cold atomic ensembles. Appl Phys Lett 98:74101. https://doi.org/10.1063/1.3555459

Larnier H, Chubak G, Schneider M, Schiffler M, Stolz R (2021) Three component SQUID-based system for airborne natural field electromagnetics. In: First International Meeting for Applied Geoscience and Energy Expanded Abstracts. Society of Exploration Geophysicists, Houston, pp 1290–1294

Legault JM (2015) Airborne electromagnetic systems – state of the art and future directions. In: CSEG Recorder, vol 40. Canadian Society of Exploration Geophysicists, Toronto, pp 38–49

LeRoux CL, Macnae JC (2007) SQUID sensors for EM systems. In Milkereit B (ed) Exploration in the new millennium: Proceedings of the Fifth Decennial International Conference on Mineral Exploration. Decennial Mineral Exploration Conferences, Toronto, pp 417–423

Letts S, Stolz R (2017) New developments in magnetic gradiometry. Exploration '17: Integrating the Geosciences: the Challenge of Discovery; Workshop: Advances in Geophysical Technologies, Toronto

Li Y, Oldenburg DW (1996) 3-D inversion of magnetic data. Geophysics 61:394–408. https://doi.org/10.1190/1.1443968

Limes ME, Foley EL, Kornack TW, Caliga S, McBride S, Braun A, Lee W, Lucivero VG, Romalis MV (2020) Portable magnetometry for detection of biomagnetism in ambient environments. Phys Rev Appl 14:11002. https://doi.org/10.1103/PhysRevApplied.14.011002

Liu H, Dong H, Ge J, Liu Z (2022) An overview of sensing platform-technological aspects for vector magnetic measurement: a case study of the application in different scenarios. Measurement 187:110352. https://doi.org/10.1016/j.measurement.2021.110352

Lucivero VG, Lee W, Dural N, Romalis MV (2021) Femtotesla direct magnetic gradiometer using a single multipass cell. Phys Rev Appl 15:64. https://doi.org/10.1103/PhysRevApplied.15.014004

Ludwig W, Eschner W, Ludwig C (1990) Planar gradiometers arranged on non-parallel surfaces for determination of a gradient tensor of a magnetic field DE4005079C2

Macnae JC (2006) Why bother with B? when you can have dB/dt?, Denver, USA

Macnae J (2012) Design and testing of armit magnetic field sensors for em systems. ASEG Extended Abstracts 2012:1. https://doi.org/10.1071/ASEG2012ab343

Macnae J (2016a) Quantifying airborne induced polarization effects in helicopter time domain electromagnetics. J Appl Geophys 135:495–502. https://doi.org/10.1016/j.jappgeo.2015.10.016

Macnae J (2016b) Quantitative estimation of intrinsic induced polarization and superparamagnetic parameters from airborne electromagnetic data. Geophysics 81:E433–E446. https://doi.org/10.1190/geo2016-0110.1

Macnae J (2017) Definitive superparamagnetic source identification through spatial, temporal, and amplitude analysis of airborne electromagnetic data. Geophys Prospect 65:1071–1084. https://doi.org/10.1111/1365-2478.12463

Macnae J, Xiong Z (1998) Block modelling as a check on the interpretation of stitched CDI sections from AEM data. Explor Geophys 29:191–194. https://doi.org/10.1071/EG998191

Maries G, Malehmir A, Bäckström E, Schön M, Marsden P (2017) Downhole physical property logging for iron-oxide exploration, rock quality, and mining: An example from central Sweden. Ore Geol Rev 90:1–13. https://doi.org/10.1016/j.oregeorev.2017.10.012

McCracken KG, Oristaglio ML, Hohmann GW (1986) A comparison of electromagnetic exploration systems. Geophysics 51:810–818. https://doi.org/10.1190/1.1442133

Meyer U, Frei M, Petersen H, Papenfuß A, Ibs-von Seht M, Stolz R, Queitsch M, Buchholz P, Siemon B (2017) HYPGEO - a collaboration between geophysics and remote sensing for mineral exploration. EGU General Assembly 2017:2442

Motchenbacher CD, Fitchen FC (1973) Low-noise electronic design. A Wiley-Interscience publication. Wiley, New York

Nabighian MN (1991) Electromagnetic methods in applied geophysics. Application/Parts A and B. Investigations in geophysics, vol 2, v 3. Society of Exploration Geophysicists, Tulsa, OK

Nabighian MN, Macnae JC (1991) 6. Time domain electromagnetic prospecting methods. In: Nabighian MN (ed) Electromagnetic methods in applied geophysics. Society of Exploration Geophysicists, Tulsa, OK, pp 427–520

Nabighian MN, Asten MW (2002) Metalliferous mining geophysics—state of the art in the last decade of the 20th century and the beginning of the new millennium. Geophysics 67:964–978

Nabighian MN, Grauch VJS, Hansen RO, LaFehr TR, Li Y, Peirce JW, Phillips JD, Ruder ME (2005) The historical development of the magnetic method in exploration. Geophysics 70:33

Oelsner G, Schultze V, IJsselsteijn R, Stolz R (2019a) Performance analysis of an optically pumped magnetometer in Earth's

magnetic field. EPJ Quantum Technol 6:634. https://doi.org/10.1140/epjqt/s40507-019-0076-9

Oelsner G, Schultze V, IJsselsteijn R, Wittkämper F, Stolz R (2019b) Sources of heading errors in optically pumped magnetometers operated in the Earth's magnetic field. Phys Rev A 99:0134201. https://doi.org/10.1103/PhysRevA.99.013420

Osmond RT, Watts AH, Ravenhurst WR, Foley CP, Leslie KE (2002) Finding nickel from the B-field at Raglan — 'To B or not dB'. In: SEG Technical Program Expanded Abstracts 2002. Society of Exploration Geophysicists, Houston, pp 404–407

Perry AR, Bulatowicz MD, Larsen M, Walker TG, Wyllie R (2020) All-optical intrinsic atomic gradiometer with sub-20 fT/cm/$\sqrt{Hz}$ sensitivity in a 22 µT earth-scale magnetic field. Optics Express 28:36696–36705. https://doi.org/10.1364/oe.408486

Poliakov SV, Reznikov BI, Shchennikov AV, Kopytenko EA, Samsonov BV (2017) The range of induction-coil magnetic field sensors for geophysical explorations. Seism Instr 53:1–18. https://doi.org/10.3103/S0747923917010078

Portniaguine O, Zhdanov MS (1999) Focusing geophysical inversion images. Geophysics 64:874–887. https://doi.org/10.1190/1.1444596

Queitsch M (2016) Modeling and inversion of airborne full tensor magnetic gradiometry data in the Thuringian basin and forest: PhD thesis, Jena

Queitsch M, Schiffler M, Stolz R, Rolf C, Meyer M, Kukowski N (2019) Investigation of 3D magnetisation of a dolerite intrusion using airborne full tensor magnetic gradiometry (FTMG) data. Geophys J Int. https://doi.org/10.1093/gji/ggz104

Rochlitz R, Queitsch M, Yogeshwar P, Günther T, Chwala A, Janser S, Kukowski N, Stolz R (2018) Capability of low-temperature SQUID for transient electromagnetics under anthropogenic noise conditions. Geophysics 83:E371. https://doi.org/10.1190/geo2017-0582.1

Rompel AKK (2009) Geological applications for FTMG. 11th SAGA Biennial Technical Meeting and Exhibition 2009:39–42

Schiffler M (2017) Processing, analysis and inversion of full tensor magnetic gradiometry data: PhD thesis, Jena

Schiffler M, Queitsch M, Stolz R, Chwala A, Krech W, Meyer HG, Kukowski N (2014) Calibration of SQUID vector magnetometers in full tensor gradiometry systems. Geophys J Int 198:954–964. https://doi.org/10.1093/gji/ggu173

Schiffler M, Queitsch M, Stolz R, Meyer HG, Kukowski N (2017) Application of Hilbert-like transforms for enhanced processing of full tensor magnetic gradient data. Geophys Prospect 65:68–81. https://doi.org/10.1111/1365-2478.12518

Schmelz M, Stolz R, Zakosarenko V, Schoenau T, Anders S, Fritzsch L, Mueck M, Meyer M, Meyer HG (2012) Sub-fT/Hz(1/2) resolution and field-stable SQUID magnetometer based on low parasitic capacitance sub-micrometer cross-type Josephson tunnel junctions. Physica C: Superconductivity and Its Applications 482:27–32. https://doi.org/10.1016/j.physc.2012.06.005

Schodde R (2017) Challenges of exploring under deep cover. AMIRA International's 11th Biennial Exploration Managers Conference, Healesville, Australia

Schodde R (2019) Trends in exploration. International Mining and Resource Conference, Melbourne, Australia

Schultze V, Schillig B, IJsselsteijn R, Scholtes T, Woetzel S, Stolz R (2017) An optically pumped magnetometer working in the light-shift dispersed Mz mode. Sensors (Basel) 17:561. https://doi.org/10.3390/s17030561

Schwindt PDD (2019) Optical beat note readout of a magnetic gradient, p 701. WE-Heraeus-Seminar, Bad Honnef, DE

Selfe GR (2009) New discovery of Ni-mineralisation in Northern Namibia Geophysical Case Study. 11th SAGA Biennial Technical Meeting and Exhibition 2009:33–38

Smirnova M, Juhojuntti N, Becken M, Smirnov M (2020) Exploring Kiruna iron ore fields with large-scale, semi-airborne, controlled-source electromagnetics. First Break 38:35–40. https://doi.org/10.3997/1365-2397.fb2020070

Smit JP, LeRoux CL (2009) TDEM survey at Shea Creek uranium deposit utilising a low-temperature superconductor SQUID. 11th SAGA Biennial Technical Meeting and Exhibition 2009

Smith R (2014) Electromagnetic Induction Methods in Mining Geophysics from 2008 to 2012. Surv Geophys 35:123–156. https://doi.org/10.1007/s10712-013-9227-1

Smith R, Annan P (1998) The use of B-field measurements in an airborne time-domain system: part I. Benefits of B-field versus dB/dt data. Explor Geophys 29:24. https://doi.org/10.1071/EG998024

Stedingk K (2012) Geologie und Erzlagerstätten im Oberharz. In: Exk.f. und Veröfftl. DGG 247, vol 247. DGG, Hannover, pp 9–81

Stedingk K, Stoppel D (1993) History of mining operations and economic importance of the Harz vein deposits. Monogaph Ser Miner Deposita 30:1–3

Steuer A, Smirnova M, Becken M, Schiffler M, Günther T, Rochlitz R, Yogeshwar P, Mörbe W, Siemon B, Costabel S, Preugschat B, Ibs-von Seht M, Zampa LS, Müller F (2020) Comparison of novel semi-airborne electromagnetic data with multi-scale geophysical, petrophysical and geological data from Schleiz, Germany. J Appl Geophys 182:104172. https://doi.org/10.1016/j.jappgeo.2020.104172

Stolz R (2015) SQUIDs in geophysics. In: Seidel P (ed) Applied superconductivity: handbook on devices and applications. Wiley-VCH, Weinheim, pp 1020–1041

Stolz R, Zakosarenko V, Schulz M, Chwala A, Fritzsch L, Meyer HG, Köstlin EO (2006) Magnetic full-tensor SQUID gradiometer system for geophysical applications. Lead Edge 25:178–180. https://doi.org/10.1190/1.2172308

Stolz R, Schmelz M, Anders S, Kunert J, Franke D, Zakosarenko V (2020) Long baseline LTS SQUID gradiometers with sub-µm sized Josephson junctions. Supercond Sci Technol 33:055002. https://doi.org/10.1088/1361-6668/ab78ba

Stolz R, Schiffler M, Zakosarenko V, Larnier H, Rudd J, Chubak G, Polomé L, Pitts B, Schneider M, Schulz M, Meyer M, Campbell K (2021a) Status and future perspectives of airborne magnetic gradiometry. In: First International Meeting for Applied Geoscience & Energy Expanded Abstracts. Society of Exploration Geophysicists, Tulsa, OK, pp 3554–3561

Stolz R, Schmelz M, Zakosarenko V, Foley CP, Tanabe K, Xie X, Fagaly R (2021b) Superconducting sensors and methods in geophysical applications. Supercond Sci Technol. https://doi.org/10.1088/1361-6668/abd7ce

Terblanche O (2008) LT SQUID Ground TEM - case studies. saga 2008

Vallée MA, Smith RS, Keating P (2011) Metalliferous mining geophysics — state of the art after a decade in the new millennium. Geophysics 76:W31–W50. https://doi.org/10.1190/1.3587224

Vengalattore M, Higbie JM, Leslie SR, Guzman J, Sadler LE, Stamper-Kurn DM (2007) High-resolution magnetometry with a spinor Bose-Einstein condensate. Phys Rev Lett 98:2023. https://doi.org/10.1103/PhysRevLett.98.200801

Venturelli M (2018) Ultra-cold atomic magnetometry:realisation and test of a87Rb BEC forhigh-sensitivity magnetic fieldmeasurements: PhD thesis, London, UK

Vetoshko PM, Gusev NA, Chepurnova DA, Samoilova EV, Syvorotka II, Syvorotka IM, Zvezdin AK, Korotaeva AA, Belotelov VI (2016) Flux-gate magnetic field sensor based on yttrium iron garnet films for magnetocardiography investigations. Tech Phys Lett 42:860–864. https://doi.org/10.1134/S1063785016080289

Webb M, Corscadden B (2009) A case study of deep electromagnetic exploration in conductive cover. ASEG Extended Abstracts 2009:1. https://doi.org/10.1071/ASEG2009ab072

Wolf T, Neumann P, Nakamura K, Sumiya H, Ohshima T, Isoya J, Wrachtrup J (2015) Subpicotesla diamond magnetometry. Phys Rev X 5. https://doi.org/10.1103/PhysRevX.5.041001

Wolfgram P, Thomson S (2018) The use of B-field measurements in an airborne time-domain system – part II: examples in conductive regimes. Explor Geophys 29:225–229. https://doi.org/10.1071/EG998225

Woods D (2010) Transient electromagnetic survey optimization using SQUID sensors. In: SEG Technical Program Expanded Abstracts 2010. Society of Exploration Geophysicists, Tulsa, OK, pp 820–823

Wu X, Xue G, Fang G, Li X, Ji Y (2019) The development and applications of the semi-airborne electromagnetic system in China. IEEE Access 7:104956–104966. https://doi.org/10.1109/ACCESS.2019.2930961

Zhang R, Mhaskar R, Smith K, Prouty M (2020a) Portable intrinsic gradiometer for ultra-sensitive detection of magnetic gradient in unshielded environment. Appl Phys Lett 116:143501. https://doi.org/10.1063/5.0004746

Zhang R, Xiao W, Ding Y, Feng Y, Peng X, Shen L, Sun C, Wu T, Wu Y, Yang Y, Zheng Z, Zhang X, Chen J, Guo H (2020b) Recording brain activities in unshielded Earth's field with optically pumped atomic magnetometers. Sci Adv 6:eaba8792. https://doi.org/10.1126/sciadv.aba8792

Zhang C, Shagieva F, Widmann M, Kübler M, Vorobyov V, Kapitanova P, Nenasheva E, Corkill R, Rhrle O, Nakamura K, Sumiya H, Onoda S, Isoya J, Wrachtrup J (2021a) Diamond magnetometry and gradiometry towards subpicotesla dc field measurement. Phys Rev Appl 15:64075. https://doi.org/10.1103/PhysRevApplied.15.064075

Zhang R, Mhaskar R, Smith K, Balasubramaniam E, Prouty M (2021b) Vector measurements using all optical scalar atomic magnetometers. J Appl Phys 129:44502. https://doi.org/10.1063/5.0037991

Zhdanov MS (2002) Geophysical inverse theory and regularization problems. Methods in geochemistry and geophysics, vol 36. Elsevier Science, Amsterdam and Oxford

Zhdanov MS (2010) Electromagnetic geophysics: notes from the past and the road ahead. Geophysics 75:75A49. https://doi.org/10.1190/1.3483901

**Publisher's note** Springer Nature remains neutral with regard to jurisdictional claims in published maps and institutional affiliations.